Magnetically tunable composite hydrogels with cellulose nanocrystals

Master's thesis
Linda Srbova

Master's Programme in Chemistry and Molecular Sciences
University of Helsinki
April 2020

Tiedekunta – Fakultet – Faculty	Koulutusohjelma – Utbildningsprogram – Degree programme
Faculty of Science	Master's Programme in Chemistry and Molecular Sciences

Tekijä – Författare – Author

Linda Srbova

Työn nimi – Arbetets titel – Title

Magnetically tunable composite hydrogels with cellulose nanocrystals

Työn laji – Arbetets art – Level	Aika – Datum – Month and year	Sivumäärä – Sidoantal – Number of pages
Master's thesis	April 2020	62

Tiivistelmä – Referat – Abstract

In this work, a series of biocompatible nanocomposite hydrogels was prepared by UV-initiated polymerization based on 2-hydroxyethyl methacrylate (HEMA), using ethylene glycol dimethacrylate (EGDMA) as a crosslinker and 2-hydroxymethyl-2-methylpropiophenone as a photoinitiator, containing liquid crystals of cellulose nanocrystals (CNCs) doped with magnetic nanoparticles. The formation of liquid crystals was achieved thanks to the intrinsic property of CNCs to self-assemble above a critical aqueous concentration. By varying the preparation conditions, allowing different times for phase-separation between the nanoparticles and CNCs and exposing the polymerization mixture to small magnetic field, films with different size and orientation of CNC liquid crystal domains were synthesized. Subsequently, the hydrogel films were studied by dynamic mechanical analysis (DMA) to evaluate the effect of these parameters on the mechanical properties, specifically the Young's modulus and the ultimate strength. Also, the microstructure of the films was studied via polarized optical microscopy (POM) and scanning electron microscopy (SEM). The water uptake capacity was also analyzed.

The results indicate that the presence of cellulose nanocrystals modulates the architecture of the prepared hydrogels. Cholesteric microdomains were embedded in PHEMA matrix and their uniaxial alignment was achieved upon exposure to small static magnetic field, already after several hours. Moreover, structural gradient in the distribution of the liquid crystalline microdomains, in dependence on their size, was obtained within the material. This originated from the direct proportionality between the size and the density of liquid crystals. Finally, it was shown that cellulose nanocrystals act as reinforcing structures of the hydrogels, when the degree of their self-assembly is sufficient, and therefore the resulting hydrogel exhibits both higher resistance to elastic deformation and also higher ultimate strength. Finally, we showed that mechanical performance of these nanocomposites can be enhanced by systematic orientation of the liquid crystalline domains.

Avainsanat – Nyckelord – Keywords

cellulose nanocrystals, magnetic nanoparticles, hydrogel, liquid crystal, PHEMA

Säilytyspaikka – Förvaringställe – Where deposited

Muita tietoja – Övriga uppgifter – Additional information

Abstract

In this work, a series of biocompatible nanocomposite hydrogels was prepared by UV-initiated polymerization based on 2-hydroxyethyl methacrylate (HEMA), using ethylene glycol dimethacrylate (EGDMA) as a crosslinker and 2-hydroxymethyl-2-methylpropiophenone as a photoinitiatior, containing liquid crystals of cellulose nanocrystals (CNCs) doped with magnetic nanoparticles. The formation of liquid crystals was achieved thanks to the intrinsic property of CNCs to self-assemble above a critical aqueous concentration. By varying the preparation conditions, allowing different times for phase-separation between the nanoparticles and CNCs and exposing the polymerization mixture to small magnetic field, films with different size and orientation of CNC liquid crystal domains were synthesized. Subsequently, the hydrogel films were studied by dynamic mechanical analysis (DMA) to evaluate the effect of these parameters on the mechanical properties, specifically the Young's modulus and the ultimate strength. Also, the microstructure of the films was studied via polarized optical microscopy (POM) and scanning electron microscopy (SEM). The water uptake capacity was also analyzed.

The results indicate that the presence of cellulose nanocrystals modulates the architecture of the prepared hydrogels. Cholesteric microdomains were embedded in PHEMA matrix and their uniaxial alignment was achieved upon exposure to small static magnetic field, already after several hours. Moreover, structural gradient in the distribution of the liquid crystalline microdomains, in dependence on their size, was obtained within the material. This originated from the direct proportionality between the size and the density of liquid crystals. Finally, it was shown that cellulose nanocrystals act as reinforcing structures of the hydrogels, when the degree of their self-assembly is sufficient, and therefore the resulting hydrogel exhibits both higher resistance to elastic deformation and also higher ultimate strength. Finally, we showed that mechanical performance of these nanocomposites can be enhanced by systematic orientation of the liquid crystalline domains.

Acknowledgment

I would like to express my gratitude to Ville Hynninen for his support and guidance throughout the whole project. I am also very grateful to Professor Olli Ikkala and Sami Hietala for sharing their outstanding expertise and encouragement. Furthermore, I wish to express my thanks to all my colleagues from the Molmat research group at Aalto, who helped me with various parts of my work. A special thanks to my partner and my mother, for their unconditional support during my studies.

Table of Contents

List of abbreviations, symbols and units

HEMA	2-hydroxyethyl methacrylate
C1 position	carbon-1 position
H-bond	hydrogen bond
CNFs	cellulose nanofibrils
BNC	bacterial nanocellulose
CNCs	cellulose nanocrystals
BC	bacterial cellulose
TEMPO	2,2,6,6-tetramethylpiperidine-1-oxyl
ζ-potential	zeta potential
Pa	pascal
LC	liquid crystals
wt. %.	weight percent
PHEMA	poly(2-hydroxyethyl methacrylate)
POM	polarized optical microscopy
vol. %	volume percentage
T	tesla
EDGMA	2-ethanediol dimethacrylate
MNPs	magnetic nanoparticles
Å	ångström
PEG	poly(ethylene glycol)
MRI	magnetic resonance imaging
FDA	Food and Drug Administration Agency
EMA	European Medicines Agency
MQ water	milli-Q water
µS/cm	microSiemens per centimeter
rpm	rounds per minute
L	liter
g	gram
°C	degree Celsius
DLS	dynamic light scattering
TEM	transmission electron microscopy

SEM	scanning electron microscopy
DMA	dynamic mechanical analysis
mM	millimolar
VSM	vibrating scanning magnetometry
Hz	hertz
Oe	oersted
K	kelvin
kV	kiloVolt
s	second
c	concentration
nm	nanometers
Pt/Pd	Platinum/Palladium
N	newton
N/min	newtons per minute
RT	room temperature
RH	relative humidity
E	Young's modulus
W_0	weight of wet sample after 4 minutes of equilibration
W_x	final weight of dried sample
Teflon	poly(tetrafluorethylene)

1. Introduction

The idea of this project originated from nature-inspired nanocomposite materials[1], such as bone[2,3], wood[2] or seashells[4], that display outstanding mechanical properties. The prominent behavior arises from the fact that they are typically composed of relatively simple components, which arrange into complex structures, and due to their synergistic effects, they give rise to strong and tough materials. Thus, our objective was to explore hydrogel-based nanocellulose nanocomposites, doped with magnetic nanoparticles, exploiting the abundance, affordable price, biocompatibility and especially the high mechanical performance of cellulose nanocrystals (CNCs).[5]

The liquid crystalline[6] self-assembly behavior of nanocellulose provides an alternative route for the manufacture of reinforced nanocomposites. Furthermore, the possibility of controlling the alignment of cellulose[7] using high static magnetic field encourages to explore alternative routes with smaller magnetic field. Finally, the mechanical and the structural properties are studied as a function of the extent of the self-assembly process and of the alignment.

Cotton-based nanocellulose and magnetite nanoparticles were chosen for the incorporation into the matrix of UV-cured poly(2-hydroxyethyl methacrylate), i.e., PHEMA. The ability of nanocellulose to self-assemble into cholesteric liquid crystals allowed for the formation of anisotropic domains of various sizes throughout the structure of the nanocomposite. Moreover, the presence of magnetically active nanoparticles induced specific response to the magnetic field. Both parameters were linked to the mechanical properties of the final films.

2. Literature survey
2.1 Cellulose

Cellulose is a fibrous, water insoluble, but biodegradable polymer, that is mainly present in higher plants, maintaining the structure of its cell walls. It can also be synthesized by specific bacteria and by certain marine animals, algae or fungi.[8]

Chemically, it is a high molecular weight homopolymer of β-1,4-linked anhydro-D-glucose units.[9] Each of its cyclic monomer units carries three reactive OH groups and is chiral, meaning that the glucose ring comprises of a carbon atom attached to four different atoms, causing the molecule to adopt a specific molecular geometry, and therefore exhibit unambiguous packing at larger scales. Each cellulose macromolecule has directional chemistry with a reducing group at the C1 position at one end (hemiacetal with pendant OH group) and a non-reducing group at C4 position on the other end. Its degree of polymerization can be up to 20 000, where wood cellulose is around 10 000 and cotton cellulose has usually around 15 000 glucose units.[10]

Cellulose is a polymorph, existing in several crystalline allomorphs with physical variations, which leads to different reactivity.[8,11] The most common is the native type I, having a parallel up arrangement, with respect to the directionality of the chain.[8,12] Regeneration or alkaline treatment of the native type cellulose I irreversibly gives the cellulose type II, with an antiparallel[12] more stable arrangement. Allomorphs of type III can be reversibly prepared by liquid ammonia treatment from both type I and II whereas type IV can be synthesized by heating cellulose type III in glycerol.[8]

Approximately 36 individual cellulose chains make up one protofibril.[13] Protofibers pack together into long slim monocrystalline microfibrils, having a structure with left-handed twist, which is caused by the intrinsic chirality of the individual building blocks.[14] The microfibrils then arrange into lattices within the cell walls.[5] Due to the chemical structure of the monomers, the cellulose chains carry a large number of hydroxyl groups. As depicted in Figure 1, these functional groups enable the formation of intramolecular and intermolecular H-bonds, which play crucial role in the formation of the organized microfibrils.[15]

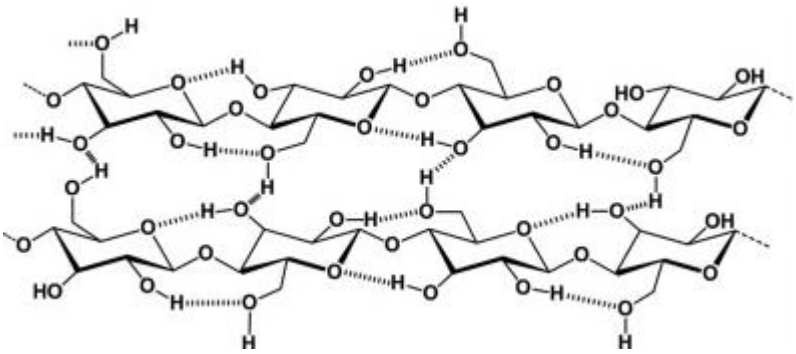

Figure 1: Structure of cellulose depicting both the intramolecular and the intermolecular H-bonds[18]

Over the process of cellulose synthesis, firstly, the intermolecular forces induce formation of glucan sheets, which then stack up onto each other making up a microfibril.[16-18] The abundant hydroxyl groups, which are present on the fibrils' surface, also represent available sites for surface modifications.[18] Yet, the complexity of the stabilizing bonds and their dense network makes cellulose insoluble in water and considerably resistant to many organic reagents. This is because the solvent molecules cannot properly penetrate the structure.[19]

Even though the cellulose microfibrils are tightly packed together, the structure is not fully crystalline (Figure 2).[20] While ordered regions are stabilized by intra- and intermolecular bonds, there are other regions where the chain order is interrupted. These dislocations or distortions of the network are caused by internal strains originating from tilting and twisting. Such cellulose regions are disordered and they can be selectively treated with acid hydrolysis. In addition, the microfibrils also tend to coalesce together. Both the disorder and the coalescence affect the macroscopic physical properties of cellulosic materials.[5]

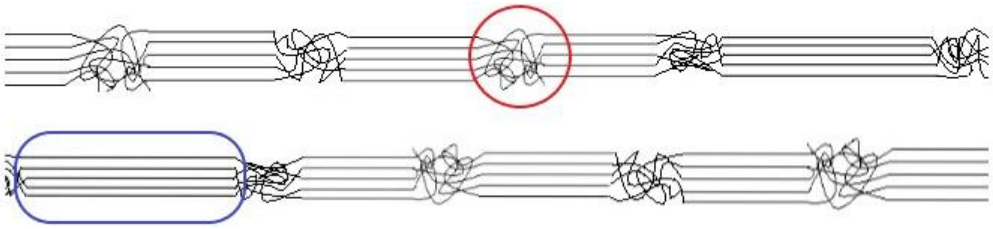

Figure 2: Section of a cellulose fiber with crystalline (in blue) and non-crystalline (red) regions highlighted

2.2 Nanocellulose

Cellulose nanostructures can be classified into 3 types: cellulose nanofibers (CNFs), bacterial nanocellulose (BNC) and cellulose nanocrystals (CNCs) (electron microscope images shown in Figure 3). All of them are biodegradable and from renewable resources. Thus, they represent interesting biomaterials with vast application possibilities.[21] While BNC is produced from 'bottom up', CNCs and CNFs are produced from 'top-down' mechanisms. A common property of CNFs and CNCs is that they demonstrate reinforcing effects in polymer nanocomposites; they however differ in length, shape, crystallinity and composition.[18]

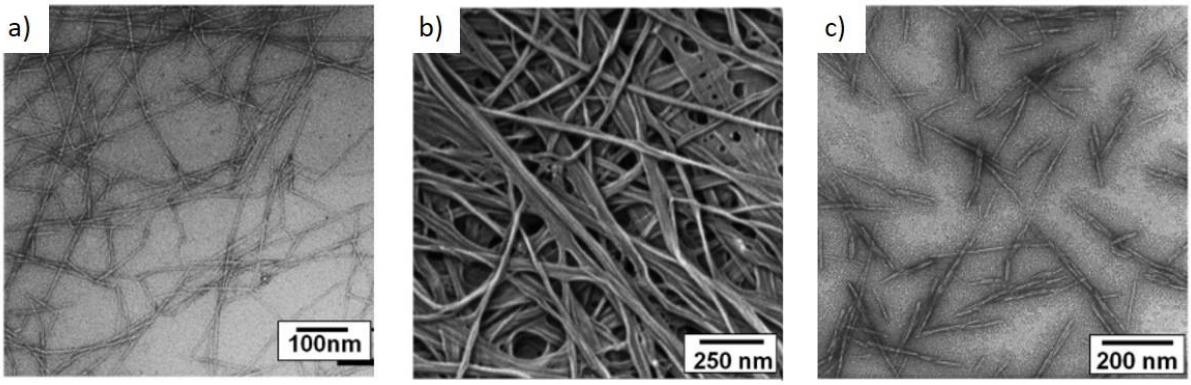

Figure 3: a) TEM image of CNFs, b) SEM image of bacterial cellulose c) TEM image of wood CNCs[21]

2.2.1 Cellulose nanofibrils

CNFs can be obtained from any raw cellulose source material, usually from wood pulp, but also from crops and other plants. They are synthesized by mechanical delamination of cell wall fibers by exposing pulp to high shear forces that rip the larger wood-fibers apart.[22] This exfoliation is achieved through high pressure homogenization, grinding, or microfluidization. Commonly, pre-treatments are conducted, mainly to minimize the energy consumption of such demanding processes[23], but they can also introduce specific properties onto the nanostructures. Such modifications can be enzymatic[24] (minimizing the energy requirements), mechanical[25] or chemical (carboxymethylation[26] or TEMPO-mediated oxidation[27]). Twisted or/and entangled nanofibrils are then obtained, usually between 5 and 40 nm wide and up to several micrometers in length. However, the exact dimensions are strongly dependent on the preparation conditions.[18]

2.2.2 Bacterial nanocellulose

Bacterial cellulose (BC) is an attractive biomaterial. Because it is synthesized by specific bacteria, its production has only negligible environmental impact.[28] The most effective producer is *Acetobacter xylinum*[28] and it gives long, highly homogeneous and thin microfibrils[29,30]. The potential of BC lies in bioapplications[31-33] and nanocomposites[34]. Similarly to other types of cellulose, fibrils contain amorphous regions, which can be selectively treated with acid.[33] However, the acid hydrolysis of BC gives nanocellulose with significantly higher crystallinity than nanocellulose from other sources.[28]

2.2.3 Cellulose nanocrystals

CNCs, also called whiskers, are rigid needle-like rods made up of highly crystalline cellulose. These structures are extracted from original cellulose fibers of bulk biomass materials (wood pulp, cotton etc.). Though, unlike in the case of CNFs, the isolation process of CNCs is chemical, using selective acid hydrolysis, usually sulphuric acid or sodium chlorite.[5]

By exposing the raw cellulose to sulphuric acid, the long glucose chains undergo degradation at the non-crystalline disordered regions, while the inflexible crystalline domains of microfibrils are retained.[35] As shown in Figure 4, controlled acid hydrolysis introduces sulphate half-ester groups onto the surface of the nanocrystals by esterification reaction of the cellulose macromolecules with the sulfate anions[5], which then become deprotonated and negatively charged, when in neutral aqueous environment. The magnitude of the nanoparticles' surface charge is expressed as ζ- potential. The numerical value of the potential indicates their stability, which originates from the electrostatic repulsion forces between the individual nanoparticles.[36]

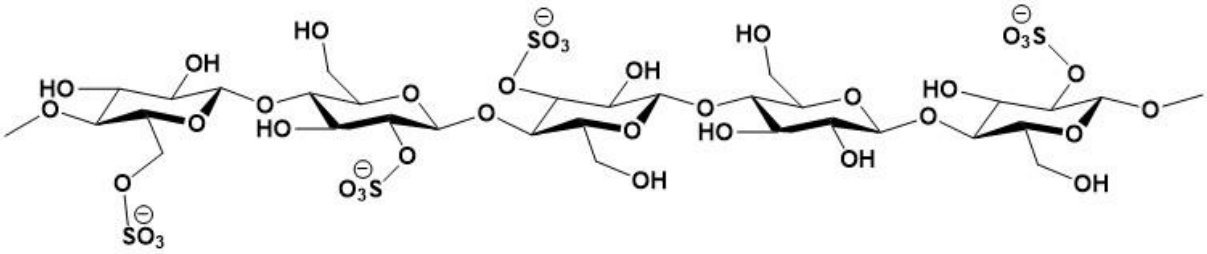

Figure 4: Cellulose with negatively charged sulphate half-ester groups on the surface

CNCs are usually 3-20 nm in diameter and only ca. 100-600 nm long, meaning that they are considerably shorter than CNFs. The specific dimensions vary depending on their source, with tunicate CNCs typically the longest.[5] In any case, CNCs are rigid structures with anisotropic shape, since their length is significantly bigger than their width. The shape anisotropy can be

quantified in form of ‘aspect ratio’, which is the ratio between the width and the length.[5] These properties are crucial for their ability to self-assemble into liquid crystals[37], which will be discussed further in Section 2.3.1.

It is due to the rich intramolecular H-bonding network and the tight packing of the cellulose chains, that CNCs are strong and rigid with excellent mechanical properties. This can be exploited in form of reinforcements for many material applications.[38-41] Their Young’s modulus along the nanocrystal’s axis is theoretically around 160 GPa[42], while experimentally it was determined to be in the range of 60-100 GPa[43] for cotton-based CNCs. The experimental values are comparable to these of Kevlar (85 GPa)[44] and E-glass fiber (73 GPa)[45], materials used to reinforce plastics. The reinforcing effect of rigid CNC structures is substantiated by the phenomenon called *mechanical percolation*[46,47], describing the formation of complex network of rods, stabilized through H-bonds between the connected CNCs[41].

The majority of CNCs’ prospective applications aims to make use of their morphology, exploiting the possibility of structural alignment, in order to improve mechanical or thermal properties of materials. CNCs have therefore high potential for applications in composites, cosmetics[48,49] or in medical field[50]. Moreover, because dried CNC films with cholesteric liquid crystals have photonic band (i.e. a frequency range where photons can’t be transmitted[51]), they also show promising optical properties for functional applications.[49]

2.3 Liquid crystals

Solids are rigid structures with constituents fixed, due to their low kinetic energy, either in a long-range (crystalline solids) or a short-range order (amorphous solids). On the other hand, molecules and atoms in gases possess such a high kinetic energy, that any order is prohibited. In normal liquids, the constituents are closer than in gases, yet they retain their constant freedom of motion.[52] Whilst crystalline solids are anisotropic materials, meaning that their properties vary with direction, amorphous solids, gases and regular liquids are isotropic and their properties do not change with direction. Interestingly, for specific liquids, under specific conditions, it is possible to achieve a state with short-range degree of molecular order that is called mesophase.[53]

Mesophase is a thermodynamically stable state of matter[53] and it is defined to be the intermediate between liquid (being fluid) and solid (with molecular order), with either translational or rotational molecular order, or both. Ordered fluid mesophases originate from non-polar or moderately polar organic compounds, or from certain amphiphilic organic compounds of geometrically anisotropic structural units.[6] Since the compounds or units contain non-identical local structural regions, at which they can interact, they can self-assemble into liquid crystals. Therefore, the formation of short-ordered structures can be observed mainly due to the anisotropy of the molecular shape. By modifying the molecular structure, certain control over the LC phases can be achieved. The average orientational order of individual molecules is described by a direction, denoted as *director*, which follows the alignment of the molecular axis of the LC-forming compounds.[54]

Based on the conditions for LC formation, two types are distinguished. *Thermotropic liquid crystals* are thermally induced and they are formed only by anisotropic molecules. On the other hand, *lyotropic liquid crystals* originate from anisotropic molecules in solvent, and they can be controlled by both, temperature and concentration.[48]

Based on the orientational arrangement and the symmetry, liquid crystals can be categorized into three main groups: nematic, smectic and cholesteric mesophases. In nematic mesophases, the molecular long axes are aligned along a preferred direction, but the long-range order of the mass centers of molecules is lacking (Figure 5a).[48] For smectic LCs, there are several classes, still, all of them show layered structure, which is due to the partial translational order of the molecules (Figure 5b and c). Smectic LCs however differ in the molecular orientation with respect to the layer normal. In cholesteric mesophases (Figure 5d), the LC structure is helical,

and it can be correlated to the arrangement of nematic LCs (that is why they are also denoted as *chiral nematic liquid crystals*), though only locally. The cholesteric structure shows periodic twisting of molecules, which are arranged in layers, having the director axis to rotate for each layer periodically.[48] The light reflected by such crystals is dependent on the pitch size, which is the distance between the layers that go the full rotation (360˚) of the director.[6]

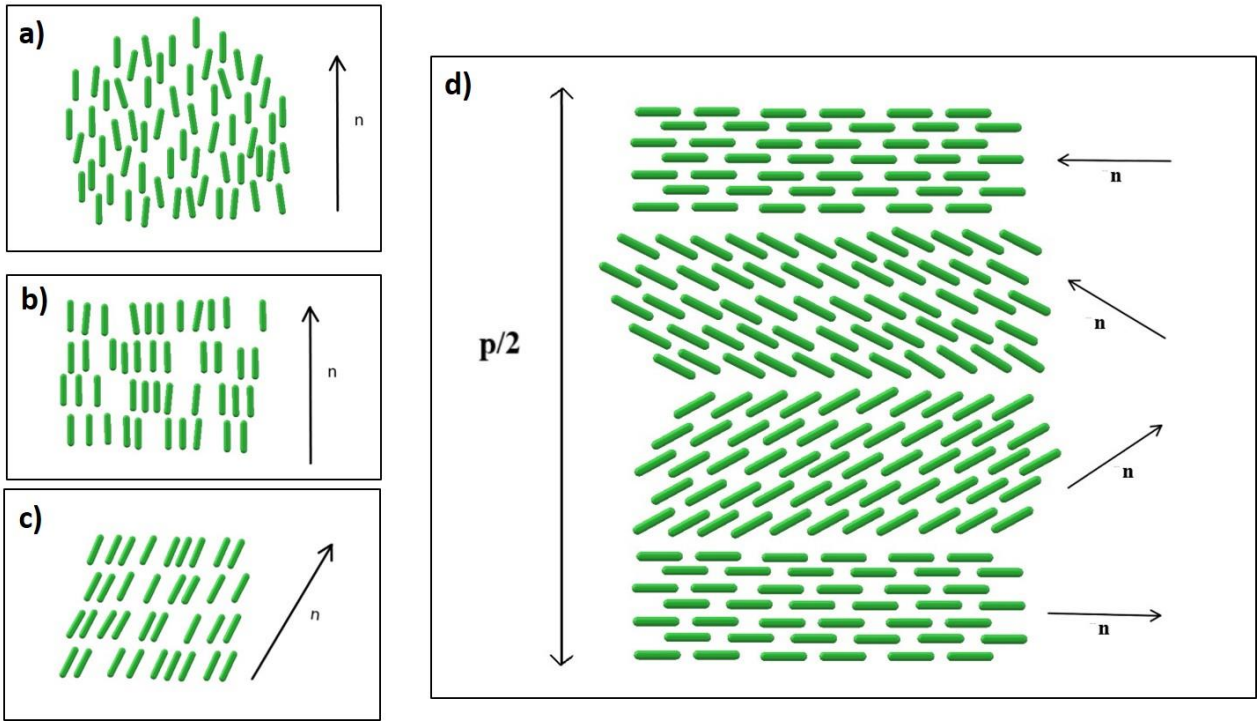

Figure 5: Schematic representation of a) nematic order, b) smectic A order, c) smectic C order and d) cholesteric order

In this project, the formation and the properties of lyotropic cholesteric liquid crystals are studied and exploited.

2.3.1 Liquid crystalline behavior of cellulose nanocrystals

2.3.1.1 Lyotropic liquid crystallinity of cellulose nanocrystals

In diluted CNC aqueous suspensions, the electrostatic repulsion among the negatively charged sulfate ester groups ensures that the CNC rods are well dispersed and randomly oriented. Naturally, charged CNCs have the tendency to minimize their electrostatics interactions.[5] When the CNC concentration in the suspension exceeds the critical value, the rods' shape anisotropy induces phase separation. This leads to the transformation of the initially isotropic liquid into a biphasic system including also anisotropic liquid crystalline regions and upon further increasing the concentration, completely liquid crystalline system is achieved.[37] Since an aqueous environment is required for the liquid crystallinity, the CNC liquid crystals are denoted as lyotropic.[6]

The critical concentration strongly depends on the CNCs' shape and on the surface charge. The threshold concentration decreases with higher aspect ratio. Similarly to that, the critical concentration decreases with the increasing repulsive forces between the particles (i.e. with higher surface charge) and vice versa.[55] For these reasons, the critical concentration value depends on the source, the synthesis conditions and the ionic strength.[7] Upon increasing the particle concentration, the size of the isolated liquid crystalline domains grow, until a continuous liquid crystalline phase can be eventually obtained.

The self-assembly process generates microscopically ordered microdomains constituting of regularly arranged cholesteric liquid crystals (Figure 6), which are separated from the isotropic phase by sharp interface, when in biphasic region.[56] The formation of the cholesteric mesophase is assumed to originate from the intrinsic chiral nature of cellulose.[57]

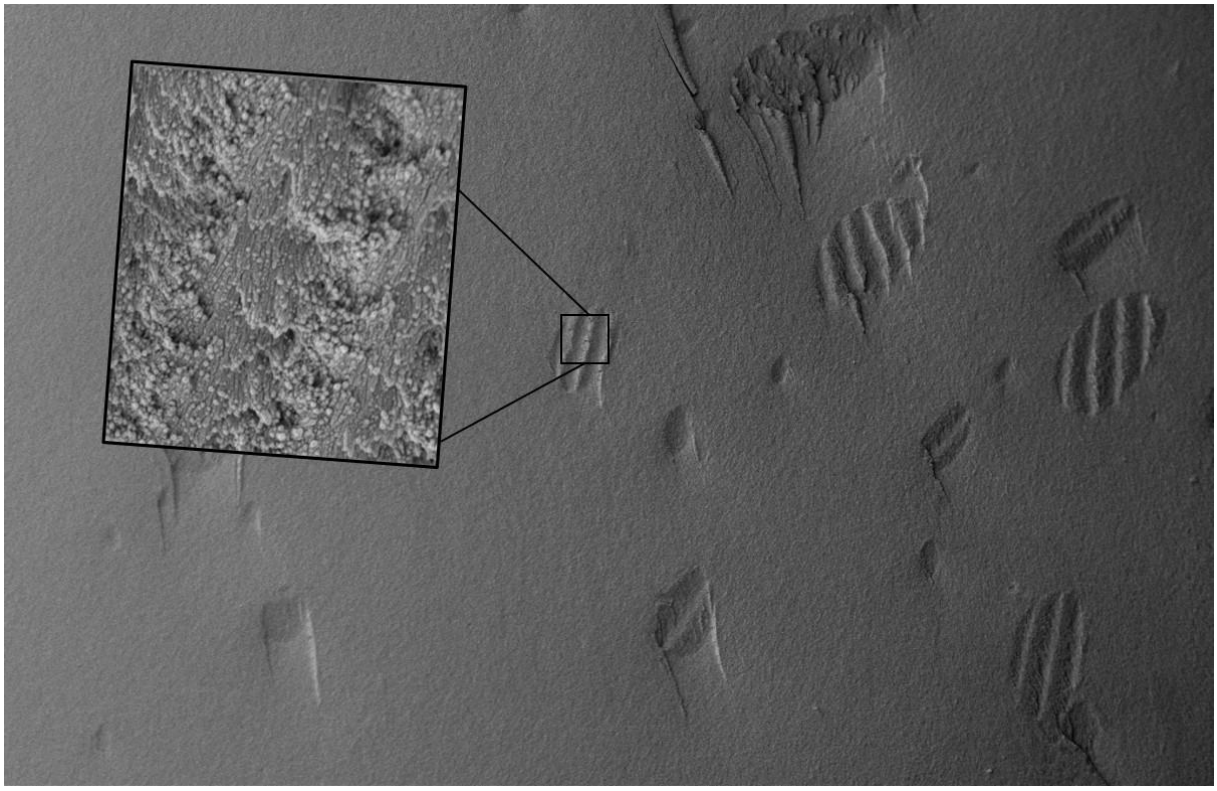

Figure 6: SEM image of PHEMA-CNC-MNP nanocomposite (7.6 wt. % CNC; 0.31 wt. % MNP), after 12 hours of equilibration on magnet before polymerized, depicts the aligned tactoids, which constitute of regularly arranged cholesteric liquid crystals of CNCs (displayed in the focus)

The isotropic and the anisotropic phase differ in the orientation of the suspended cellulose nanoparticles. Since LC phases anisotropically refract light, they appear birefringent when observed under polarized optical microscopy (POM) with crossed polarizers (Figure 7).[58]

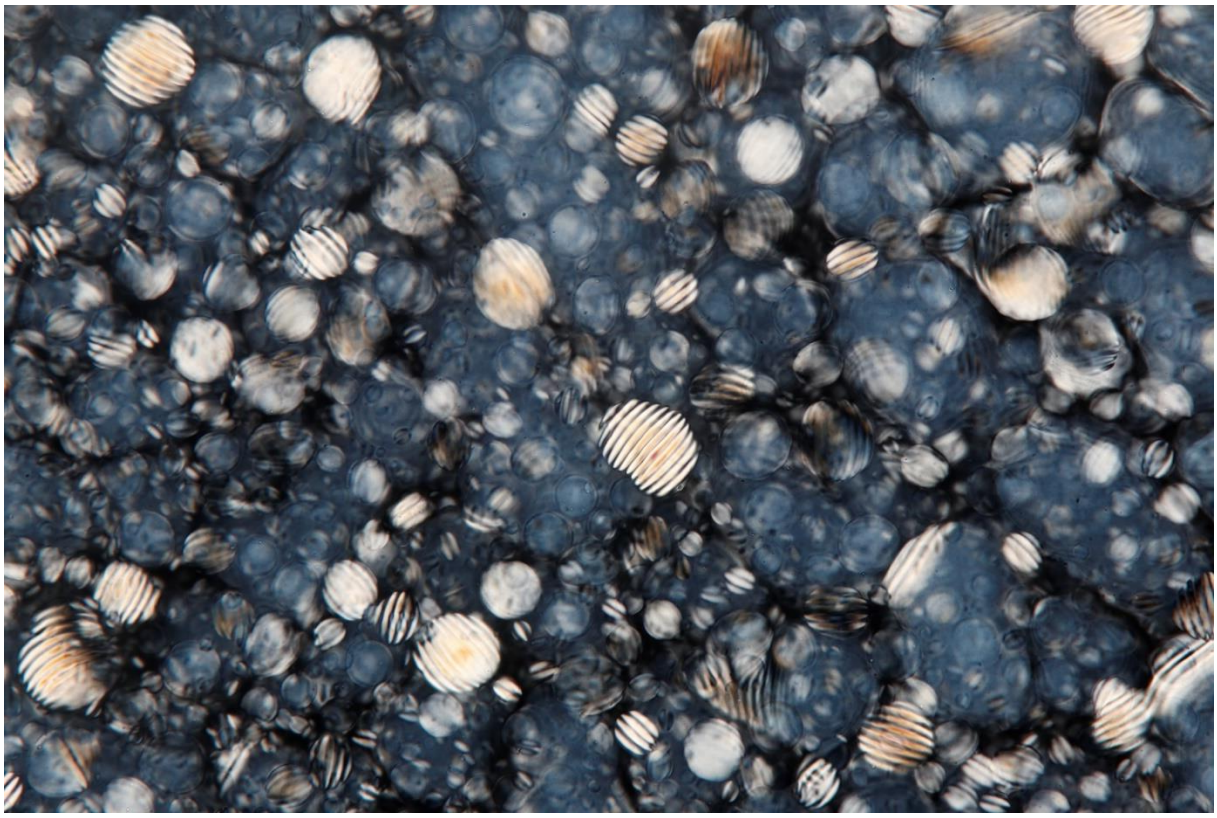

Figure 7: POM image of PHEMA-CNC-MNP film (7.2 wt. % CNC and 0.3 wt. % MNP), equilibrated for 24 hours before polymerized, depicts birefringent anisotropic regions of CNC tactoids, which are sharply separated from the dark isotropic

The phase-separation process of CNC suspensions, over gradually increasing cellulose concentrations, was studied by Ureña-Benavides E. et al.[59]. They determined the critical concentration for phase-separation of cotton-based CNC to be around 3.0 vol. %. The viscosity of the suspension increased significantly between 7 - 10 vol. % and when observed with naked eye, the samples were thought to adopt fully cholesteric organization as they appeared birefringent. Yet, the POM still revealed presence of isotropic regions. Both Ureña-Benavides E. et al.[59] and Lagerwall J. PF et al.[49] have shown that filter-paper derived CNC suspensions of higher concentrations (around 15 vol. %) were highly viscous and a transition from liquid crystalline state to gel-like glassy state was observed. Lagerwall J. PF et al.[49] have concluded that it results from the physical gelation phenomenon and that system of such high CNC concentrations can display only the degree of order, which the structure achieved to adopt prior to this transition. That is why the high viscosity of concentrated CNC suspensions is an obstacle for studies of the phase-equilibration behavior.

2.3.1.2 Self-assembly and tactoids

Resulting from the intrinsic chirality of cellulose molecules, CNCs have the ability to self-assemble into left-handed helicoids, which then give rise to microdomains of regularly ordered nanoparticles. Such a self-assembly of CNCs is observed only when the concentration is sufficient.[37] The initial liquid crystalline microdomains appear in form of discrete droplets, denoted as 'tactoids', showing specific fingerprint texture of periodic birefringent bands, spontaneously nucleating from the aqueous CNC suspension. The bands originate from the helical rotation of the layers and the distance between two neighboring bands is the distance between two layers, over which the director rotates 180˚, i.e. half-pitch. The pitch (full rotation 360˚ of the director) determines the wavelength of the light that is reflected by such crystals.[6] The fingerprint pattern can be observed by POM under crossed polarizers. By increasing the CNC concentration[49] or by allowing longer time for the suspension to phase separate, bigger tactoids with more birefringent bands are formed. The isotropic-to-chiral nematic phase equilibrium and the pitch size is also sensitive to the temperature, to the presence and to the nature of the counterions in the suspension.[49] Eventually, when the tactoids are big enough, they can also grow by coalescence, meaning that smaller tactoids fuse to form larger ones (see Figure *8*).[60]

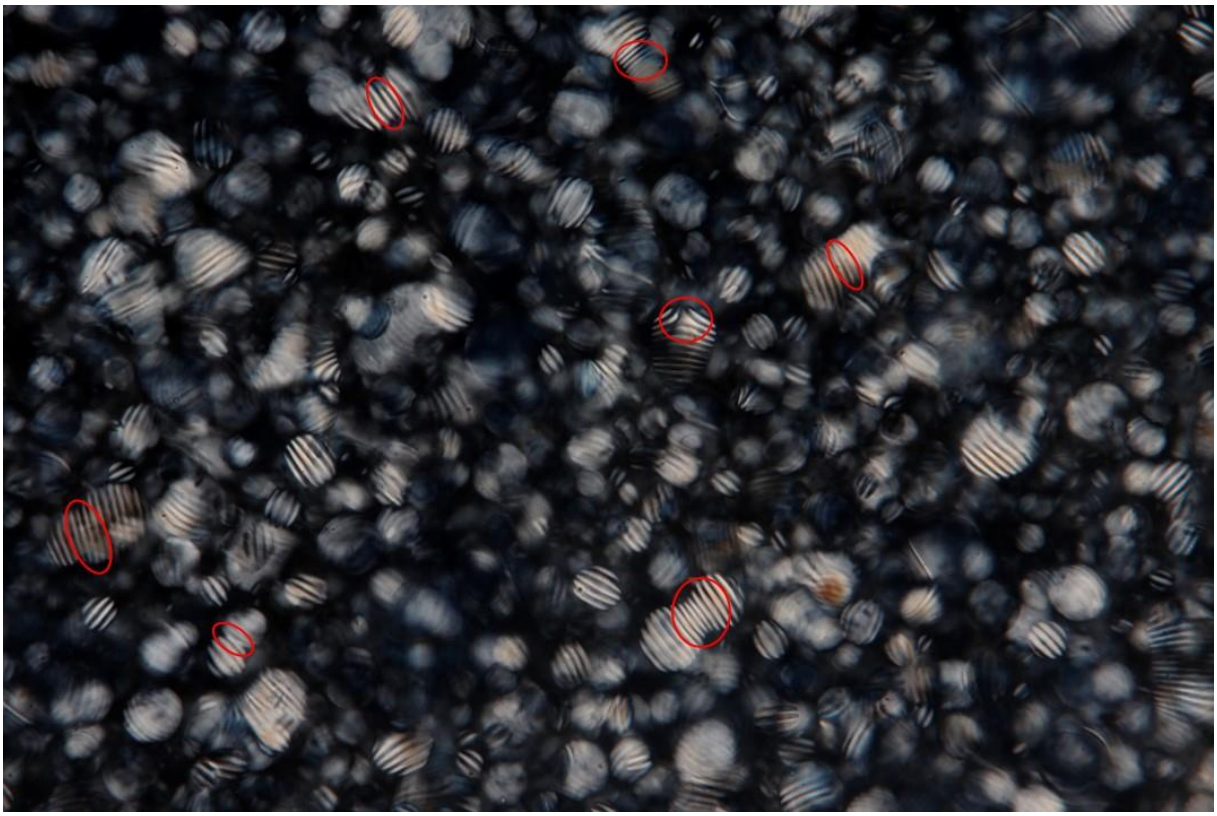

Figure 8: POM image of PHEMA-CNC-MNP film (7.4 wt. % CNC and 0.4 wt. % MNP)

As it can be seen in Figure 7 and Figure 8, chiral nematic structures of CNCs can be retained and visualized in form of solid films, by locking the LCs in the helical arrangement by drying a thin layer of suspension.[37] Likewise, by embedding the nanoparticles in a polymer matrix, it is possible to capture cellulose liquid crystals within the material structure. Subsequent freeze drying of the material allows for visualization of individual CNCs within the tactoids by scanning electron microscopy (SEM), as it was done for the specimen in Figure 6. This is feasible because the helical arrangement of nanocrystals becomes trapped in the matrix, and so the crystalline structure does not collapse.[60,61]

2.3.1.3 Magnetic response of nanocellulose liquid crystals

CNCs are particles that manifest negative diamagnetic anisotropy.[7] This means that the CNC nanorods have the ability to orientate perpendicularly to the direction of the external magnetic field, placing the cholesteric axis in the direction of the field.[7,62]

It has been demonstrated that dilute suspensions of tunicate-derived CNCs start to respond to strong magnetic fields (7 T) already after few minutes.[58] Even better than that, it has been proven that it is possible to align the cotton-derived CNCs using only relatively weak magnetic fields (0.56 T), over reasonable time scales. Yet, suspensions of high CNC concentrations are necessary, in order to achieve the alignment under low magnetic fields, as the Brownian motion of the nanocrystals effectively induces relaxation of the particles.[7]

It is therefore evident, that CNCs from different sources have different properties, such as different aspect ratios (higher for tunicate CNCs over cotton[21] - lower concentrations are sufficient), crystallinity (also higher for tunicate-based CNCs[21]) and surface charge (causing different diamagnetic susceptibility). This has significant implications on the behavior of chiral nematic suspensions of cellulose of different origins.

In summary, having the possibility to control the CNCs' orientation using magnetic field in a reproducible manner gives us a good platform for the development of novel CNC-based materials. Still, it would be useful to develop methods for alignment using smaller magnetic field strengths. For that purpose, we will use additional magnetic nanoparticles, to be discussed later.

2.4 Hydrogels

Hydrogels are soft rubbery-like hygroscopic polymeric networks swollen with water. The water permeability and strong hydrophilicity makes them to possess particularly interesting properties, often compatible with of living tissues.[63] Thus, when considering inert hydrogels, they represent attractive materials for biomedical applications such as matrices for regenerative medicine[64] or cell encapsulation.[65-67] Yet, when compared to other types of materials, synthetic hydrogels typically show rather weak mechanical properties.[68]

Based on the nature of the hydrogel network, hydrogels can be either physical or permanent (also called as chemical). The former type consists of entangled chains, held together by secondary forces, while the latter is formed by covalent crosslinking of the network.[67] Moreover, hydrogels can show either homogeneous network mesh sizes or the meshes can involve heterogeneous size distribution, or even macroporous sizes. The level of their transparency depends on the nature of their morphology. While homogeneous gels are visually clear due to the absence of heterogeneities, macroporous hydrogels are typically not transparent (often opaque or even white), which is caused by the presence of large amount interconnected pores that scatter light.

2.4.1 Poly(2-hydroxyethyl methacrylate) hydrogel

Poly(2-hydroxyethyl methacrylate) (PHEMA) is a bioinert polymer made from vinyl monomer 2-hydroxyethyl methacrylate (HEMA), their chemical structures are depicted in Figure 9. Wichterle and Lim[63] were the first to suggest PHEMA to be suitable for bioapplications and only few years later Wichterle[69] patented PHEMA hydrogel for soft contact lenses.

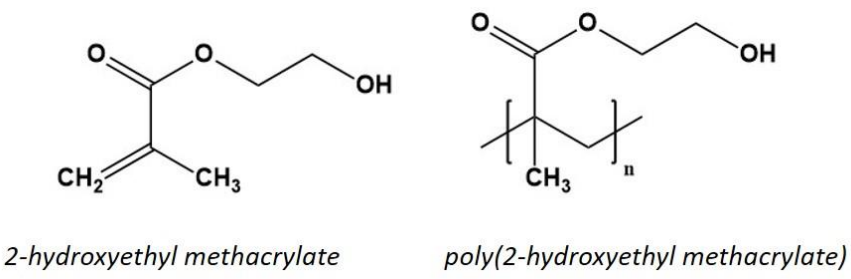

Figure 9: Chemical structure of 2-hydroxyethyl methacrylate and poly(2-hydroxyethyl methacrylate)

HEMA monomer can be polymerized by various mechanisms, but for the purpose of this project, PHEMA prepared by free-radical photopolymerization at room temperature will be discussed, using water as solvent.[70] Through this procedure, a soft, flexible, water-absorbing plastic is obtained. Besides the monomer, the polymerization mechanism also uses using ethylene glycol dimethacrylate (EGDMA) as crosslinker and photoinitiator, both displayed in Figure 10. Photoinitiator is a photoactive molecule that absorbs energy of photons. Upon the exposure to the electromagnetic radiation, with wavelengths in the UV range, its bonds undergo dissociation and the decomposition process gives rise to radicals. These primary radicals then attack either the HEMA or the crosslinker monomers, initiating the polymerization reaction. Following the scheme in Figure 11, the growing process of the polymer proceeds by repeated addition of HEMA or EDGMA monomers onto the growing center, while after each step, the growing radical center moves onto the last unit.[71]

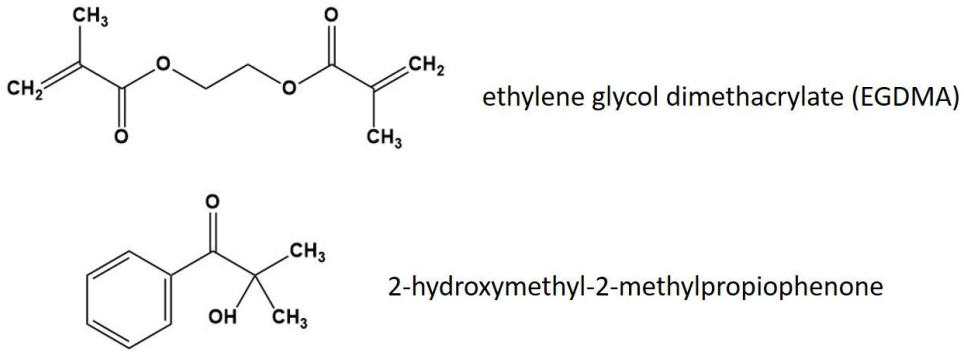

Figure 10: Chemical structure of EGDMA used as crosslinker and 2-hydroxymethyl-2-methylpropiophenone used as initiator

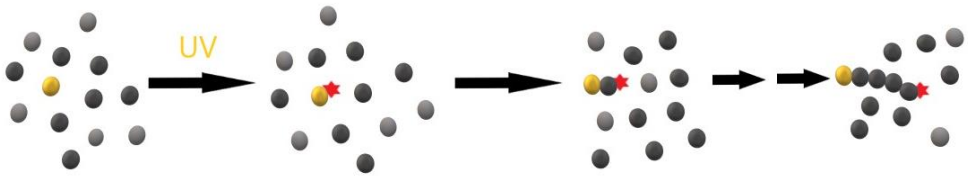

Figure 11: Scheme of photo-initiated radical polymerization, where the photoinitiator molecule is shown as a yellow ball, the HEMA monomers and EGDMA molecules are in grey or black, and the primary radical/growing center is marked with the red star

In case of polymerization in solution, if the water content is above the equilibrium capacity of the hydrogel, a phase-separation process takes place, giving rise to pores within the structure.[63] But also other factors influence the degree of the porosity (see Section 2.4.).

HEMA monomer and the photoinitiator are fully water-soluble. And even though EGDMA has low solubility in water, the presence of soluble HEMA helps the dispersion of the crosslinker

in the aqueous polymerization medium.[66] However, over the polymerization process, the initially soluble components create water insoluble, yet hydrophilic, PHEMA network.[72,73] This sudden change in solubility of the environment induces phase separation between the macromolecules and water, causing the network to self-assemble and form voids.[67] Visually, it can be observed when water content is around 45 wt. %, because the initially transparent solution turns turbid. When the water content is increased further, eventually a rather non-transparent amorphous hydrogel is acquired. The water molecules are either 'bound' or 'free' within the pores. The water is absorbed into the interstitial space and the fraction therefore determines the absorption capacity of the hydrogel.[67] Scanning electron microscopy can be used to study the morphology of the hydrogel structure.

2.4.2 Hydrogel nanocomposites

Nanocomposites are materials consisting of homogeneously dispersed nanoscale reinforcements within a matrix. To overcome the mechanical weakness of hydrogels, it has been suggested that the incorporation of molecules, which can adopt certain degree of molecular order, could lead to the enhancement of their mechanical properties.[74] This could be achieved for instance by copolymerization with crystalline or liquid crystalline moieties.

2.5 Magnetic nanoparticles

Colloidal suspensions of magnetic nanoparticles (MNPs) in a carrier liquid are called ferrofluids. Depending on their chemical composition and nanoscale dimensions, magnetic nanoparticles can have either permanent magnetic moment or, when at a very small nanoscale dimensions (ca. 100 Å), the individual particles represent single magnetic domains.[75] The latter case renders them the outstanding property of being superparamagnetic. This means that without the presence of external magnetic field, they do not show any magnetic moment, but they display a large magnetic response when exposed to magnetic field.[76] Yet, the size of the nanoparticles is critical for the magnetic properties of the ferrofluid. Undesirably, the magnetic interactions promote their tendency to agglomerate especially when in vicinity of an external magnetic field gradient. Thus, to assure the colloidal stability of magnetic fluids, the prevention of their aggregation is required. For this reason, the particles are functionalized with molecular ligands or surfactants so that the formation of irreversible aggregates is effectively hindered. Moreover, such coatings also enhance the chemical stability, or they may contain functional

groups which enable bonding with specific molecules. Typical coating layers are composed of small molar mass organic molecules (such as citric acid[77]), polymers (such as dextran[78], PEG[79]) or inorganic compounds (silica[80]). These species adsorb on the nanoparticles surface either by physical interaction (e.g. Coulombic attraction or van der Waals forces) or through chemical bonds with the active sites. The desired coatings are obtained by appropriate synthetic procedures[81] while better stability can be achieved with thicker coatings due to bigger spacing between the magnetic domains.

Due to the MNPs' distinguished properties, they are used in variety of applications ranging from audio or optics devices to biotechnology or biomedicine, for instance in loudspeakers[82], biomolecule separation[83], in targeted drug delivery[81], in cell labeling or in magnetic resonance imaging (MRI)[84], where they act as contrast agents. Most of these applications take advantage from the fact that iron oxide MNPs are rather non-toxic, chemically stable, uniform and well dispersed. In the proximity of magnetic field, the superparamagnetic grains arrange themselves along the direction of the external field so that their moments align and a chain-like structure is created[85]. Such arrangement of magnetic nanoparticles is exploited in this project.

Iron oxide-based magnetic nanoparticles are common. It is because they greatly withstand oxidizing conditions, they have good magnetic properties and on top of that, they have low toxicity. Their negligible negative effects on organism have also been recognized by the Food and Drug Administration (FDA) and the European Medicines Agency (EMA), and so the use of magnetite MNPs has been successfully approved in the medical sector.[81]

2.6 Nanocomposite materials

Nanocomposite materials are defined as hybrid materials where at least one of the components is of nanoscale. Therein it is aimed that the properties are significantly improved from those of the original materials, i.e., display synergy leading to enhanced mechanical performance.[86] They are often anisotropic, meaning that their physical properties vary along different axes, both in natural and man-made materials.[86,87]

More specifically related to the present work, the presence of cholesteric liquid crystals can lead to outstanding mechanical properties of certain tissues and biological nanocomposite materials.[48,88] It is related to the helical structure, that is present within the matrix, which can dissipate the fracture energy and therefore provides the high fracture toughness for the material (lobster cuticle[89]or dactyl club[90]). Tatsumi et al.[91] and MacLachlan et al.[60] have shown that liquid crystalline helical structures of CNCs can be successfully retained in certain polymer matrices by conducting photopolymerization of precursor aqueous suspensions.[49] Also, by incorporating the CNC tactoids within a polymer matrix, the complex structure of natural very tough materials (such as nacre) are mimicked, which may lead to the development of novel functional polymer nanocomposites of desired mechanical properties. Moreover, in another publication, MacLachlan et al.[92] have shown that when exposing the CNC suspensions doped with MNP to external gradient magnetic fields, the phase separation process can give discrete liquid crystalline tactoids with chiral nematic bands unidirectionally aligned along the magnetic field.

By combining the concepts mentioned above, novel cellulose-based nanocomposite hydrogels with of controllable mechanical properties could be designed.

3. Aims

In this research we aimed to explore control over the orientation of liquid crystalline microdomains of cellulose nanocrystals and subsequently incorporate such ordered system into soft hydrogel material. The intention is to design nature-inspired nanocomposite material with controllable mechanical properties, which would be non-toxic and biocompatible.

Firstly, the ability of cotton-based nanocellulose to self-assemble into liquid crystals (LC) by phase separating in aqueous environment will be analyzed and the possibility of controlling the orientation of LC using superparamagnetic nanoparticles by weak external magnetic fields will be exploited. The ordered mesophases of CNCs will be then embedded in PHEMA matrix by conducting UV-induced polymerization of the precursor aqueous suspension.

The extent of phase-separation process of nanocellulose and the orientation of the anisotropic phase in the system would be determined by the synthesis conditions and monitored using optical microscopy. The formation of ordered and aligned regions in the hydrogel specimens would be examined by different electron microscopy techniques. Ultimately, the conceivably reinforcing effect of the periodically arranged cellulose nanocrystals would be investigated through tensile measurements. Moreover, the varying cellulose distribution could lead to differences in water uptake between various hydrogels.

In this project, the focus is on specific features of nanocomposite hydrogels which contain liquid-crystalline structures and superparamagnetic nanoparticles.

4. Experimental

4.1 Chemicals

Sulphuric acid, ferric chloride hexahydrate, ferrous chloride tetrahydrate, ammonium hydroxide, nitric acid (68-70%), diethyl ether, sodium citrate as a stabilizer, acetone, 2- hydroxyethyl methacrylate (HEMA) as a monomer, ethylene glycol dimethacrylate (EGDMA) as a crosslinker and 97% 2-hydroxymethyl-2-methylpropiophenone as a photoinitiator were purchased from Sigma Aldrich and used without any further purification. Deionized Milli-Q (MQ) water was obtained from Milli-Q water system, Millipore.

4.2 Preparation of cellulose nanocrystals

Whatman filter paper Grade 1 (Cat no 1001125) was cut into 1cm^2 squares and then ground using the Wiley mill to obtain 45 g of paper powder. The powder was mixed together with 848 mL of a 56 % sulphuric acid in a round bottom flask with a stirring rod. The flask with suspension was placed in a 45 °C water bath for 45 minutes, stirring at 45 rpm inducing the degradation of the cellulose fibers at the amorphous regions. Subsequently, the milky solution was diluted with 6 liters of MQ water in a beaker and was let to sediment overnight. The supernatant was then removed, the white thick sediment below was divided into tubes and centrifuged at 7000 g for 20 min at room temperature. The created supernatant was again discarded, the CNC sludge was slightly diluted with water and centrifuged again at 1000 g for 45 minutes at room temperature. Again, the supernatant was carefully removed and the white thick solution was dialyzed against MQ water for several days, until there were no white clumps present and the conductivity of the solution was below 5 µS/cm. Finally, the cloudy liquid was filtered under vacuum using Buchner flask and Whatman paper no 532.

A stable cellulose suspension of approximately 5 wt. % was obtained. It was further concentrated using rotary evaporator under 65 °C water bath, until the concentration reached 14 wt. %. The concentration process caused aggregation of the crystal rods and thus it had to be sonicated for 10 minutes to disperse the nanoparticles and to obtain a homogeneous suspension.

4.3 Preparation of magnetic nanoparticles

The water-based magnetic fluid was prepared by a co-precipitation method from ferric ($FeCl_3$) and ferrous salt ($FeCl_2$) in alkali medium (ammonia hydroxide) and sodium citrate was used as stabilizer for the nanoparticles. The process followed the modification of protocols of Massart, Rene[93] and Talbot, Delphine, et al.[94]

The magnetite was prepared by dissolving 43.25 g $FeCl_3 \cdot 6H_2O$ and 15.9 g $FeCl_2 \cdot 4H_2O$ in 1440 ml MQ water and fast addition of 160 ml precipitant agent NH_4OH followed. First, the solution was vigorously stirred over 5 minutes at 400 rpm, and afterwards the supernatant was discarded by decantation using a permanent magnet that enabled the control of the precipitate. Subsequently, 39 mL of HNO_3 (68-70 %) were added onto the black precipitate, to oxidize the nanoparticles, and the volume was then filled up to 300 mL by MQ water. The solution was stirred at 400 rpm for 30 minutes and decanted with magnet. The black particles were washed three times with acetic acid and with diethyl ether, then 110 ml of distilled water were added, and the remaining ether was removed by heating up the solution to 40 °C. The particles were prevented from the aggregation by the addition of 3.9 g of sodium citrate and stirred for 30 minutes at 80-100 °C. At room temperature, the solution was again washed twice with acetone and twice with ether, then re-dispersed with the desired volume of water and again, remaining diethyl ether was evaporated. The chemical reaction of the MNPs' synthesis is given in Figure 12. Finally, filtration using 0.2 µm filter paper was carried out and the resulting concentration was determined gravimetrically.

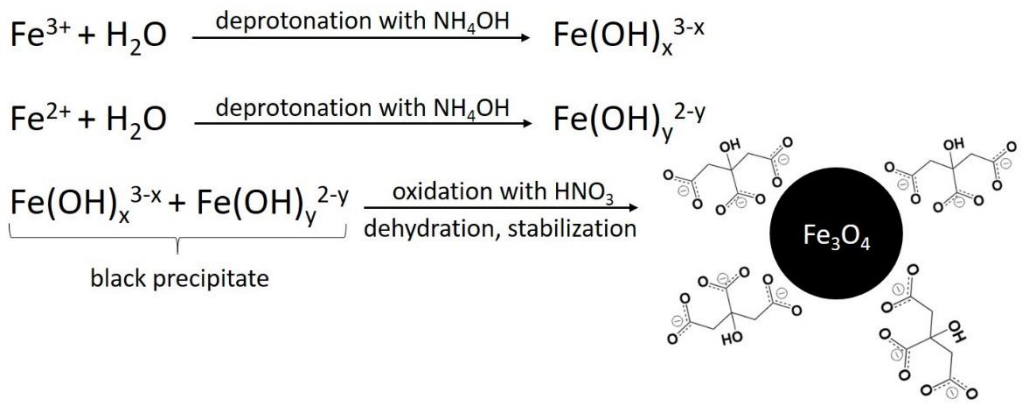

Figure 12: Scheme showing the reaction mechanism of citrate-stabilized magnetite nanoparticles from an aqueous mixture of iron(III) and iron(II) chloride salts[109]

4.4 Preparation of poly(2-hydroxyethyl methacrylate) composite hydrogel

The hydrogel samples containing CNCs and MNPs were prepared by UV initiated radical polymerization of monomer mixtures. Also, a reference sample without any CNCs was prepared. The sample codes and their preparation conditions are indicated in Table 1.

The CNC suspension (14 wt. %) was mixed with HEMA stock solution (monomer, crosslinker and initiator) and with MNP dispersion (84 wt. %). The specific contents of chemicals for each type of sample are listed in Table 2. The dispersions were then thoroughly sonicated, until no clumps were observed. Volume of 900 µL was transferred into quartz glass cuvette, sealed with Teflon tape, purged with Argon, carefully closed and taped to minimize the content of oxygen inside the flask, which would inhibit the polymerization. Subsequently, the cuvette was positioned horizontally as shown in Figure 13, to enable the mixture to cover one full side, to give the desired rectangular shape of the thin film.

Table 1: Denotation of individual specimens, their composition and the preparation parameters

sample name / conditions	**starting solution**		**TIME allowed to form tactoids (hours)**	**alignment on Magnet**
	PHEMA&MNP = Hydrogel matrix	**CNC**		
H	X		0	
HC	X	X	0	
HC_4h	X	X	4	
HC_{mg}_4h	X	X	4	X
HC_15h	X	X	15	
HC_{mg}_15h	X	X	15	X

Table 2: Hydrogel nanocomposites from different starting mixtures –composition in weight percentage

sample/chemical	**HEMA wt. %**	**EDMA wt. %**	**initiator wt. %**	**Pure CNC wt. %**	**pure MNP wt. %**	**water wt. %**
H	39.82	0.11	0.04	-	0.73	59.31
HC_{mg}_4/15h	39.82	0.11	0.04	8.28	0.73	51.02

Samples *HC* and *H*, hydrogels with or without CNCs, respectively, were exposed to UV directly after filling up the cuvette. Samples *HC_4h* and *HC_15h* were allowed to equilibrate on flat surface for either 4 or 15 hours, before placing into the UV lamp. Whilst specimens denoted as HC_{mg}*_4h* and HC_{mg}*_15h* were placed for either 4 or 15 hours onto a rectangular magnet, before polymerizing with UV (Figure 13). All the suspensions were photopolymerized over 3 hours in a UV chamber and thin films were obtained.

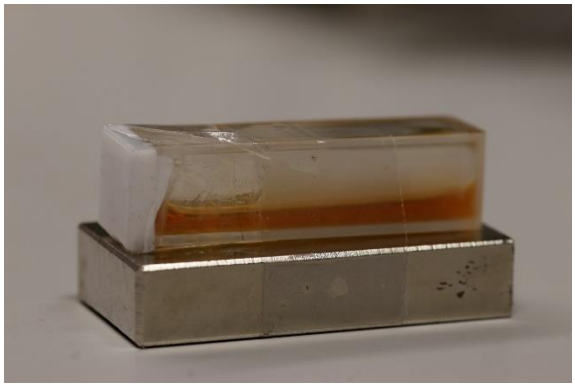

Figure 13: Reaction mixture placed horizontally on a rectangular magnet to allow alignment of the CNC tactoids

The formed hydrogel films were then carefully removed from the cuvette mold using a spatula, washed in water over several days, to remove all the unreacted components and stored in MQ water at room temperature until use.

The permanent magnets used in this projects were Neodymium N40 (NdFeB) with nickel-plated coating, cuboid in shape, with the longitudinal direction almost equal (only few millimeters longer) to the height of the cuvette (see Figure 13). As depicted in Figure 14, the individual magnets created inhomogeneous magnetic fields ranging from 65 mT in the center, up to 500 mT on the sides.

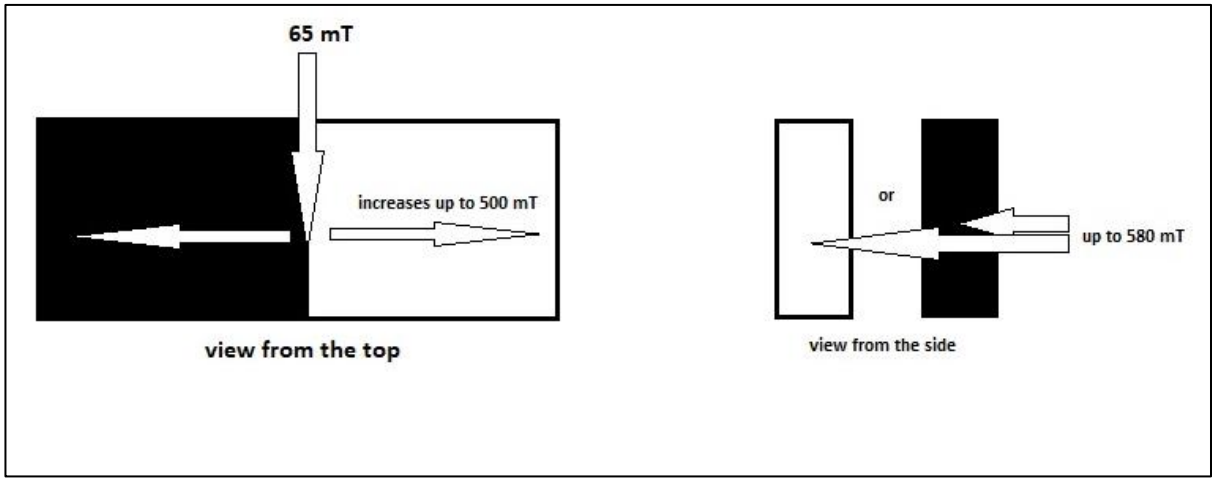

Figure 14: The strength of the magnetic field produced by magnets which were used in this project

4.5 Characterization

The morphology and the surface charge of CNCs and MNPs was studied with DLS and TEM. The tactoids' arrangement within the matrix and the morphology of the final nanocomposite hydrogels was analyzed using POM and SEM. The mechanical properties were studied by dynamic mechanical analysis (DMA) that provided information on the tensile properties. Also, the water uptake of specimens was evaluated.

4.5.1 Dynamic light scattering and zeta (ζ) potential

Dynamic light scattering (DLS) and zeta (ζ) potential measurements were done using a Malvern Zetasizer Nano ZS90, Malvern Instruments. Polystyrene cuvettes (product no. DTS0012, Malvern Instruments) and folded capillary zeta cell cuvettes (product no. DTS1070, Malvern Instruments) were used for DLS measurements and for zeta potential measurements, respectively. The suspension concentrations (both CNC and MNP) were 0.01 wt. % in 1.0 mM NaCl, reducing the repulsive interaction between the particles.[95] Measurements were made at room temperature.

4.5.2 Vibrating sample magnetometry

The vibrating sample magnetometry (VSM) was used to examine the superparamagnetic properties. The hysteresis loop of the MNPs was obtained by using a Quantum Design PPMS VSM vibrating sample magnetometer. The measurement was performed using standard polypropylene cups containing 5–7 mg of the powder sample of MNPs. The vibrational frequency and amplitude were set to 40 Hz and 1 mm, respectively, between -10 000 and 10 000 Oe (-1 T and 1 T) at 300 K.

4.5.3 Transmission electron microscopy

Transmission electron microscopy (TEM) imaging of CNCs and MNPs was carried out using JEM-2800 (JEOL) high-resolution TEM microscope at 200 kV.

First, the TEM flat 200 mesh copper grids with holey carbon support film (Electron Microscopy Sciences) were plasma cleaned (30 s, Gatan Solarus 950) in order to remove the impurities of the surface and to ensure perfectly clean and uncontaminated conditions for the analysis. Small volume (3 µL) of highly diluted suspension of CNC or MNP (c = 0.01 wt. %) was pipetted on the clean grid and incubated for 1 minute at RT so that nanoparticles could attach to the grid. Subsequently, the water was gently blotted using the edge of a filter paper and allowed to completely dry under ambient conditions.

4.5.4 Scanning electron microscopy

The formation of CNC liquid crystals and the hydrogel structure was investigated by scanning electron microscopy (SEM). Thin specimens cut from the prepared hydrogels were first dried on air and then they were snap frozen by immersion into liquid nitrogen and subsequently lyophilized. The freeze-drying process provided a suitable preparation process for the investigation of the liquid crystalline and hydrogel morphologies. To be able to observe the inner structure, the arrangement and the alignment of the CNC tactoids, a section of the dried gel was cut with a scalpel or broken off and mounted on a metal stub with a carbon tape so that the desired part could be analyzed. The sample was coated with 6 nm thick layer of Pt/Pd alloy using a Leica EM ACE600 high vacuum sputter coater prior to imaging to ensure conductivity of the sample and to minimize the charge buildup on the surface.

The SEM images were obtained using Zeiss Sigma VP scanning electron microscope at 1.5 kV acceleration voltage.

4.5.5 Polarized optical microscopy

Polarized optical microscopy (POM) analysis was conducted using Leica DM4500P high-end polarization microscope with transmitted light using crossed polarizers combined with a Canon EOS 80D DSLR camera.

The POM samples were prepared by placing a small volume of the analyzed suspension inside a Secure Seal imaging spacers (Grace Bio-Laboratories inc.,USA), which were attached on a microscope glass slide. The suspensions were then protected with a cover glass and the specimen was let still to allow the formation, growth and possible alignment of liquid crystals.

In the case of HEMA-CNC-MNP suspensions, the samples were also polymerized by placing into the UV lamp for 3 hours before studying by POM and the effect of the presence of superparamagnetic specimens on the behavior of the liquid crystals was studied.

4.5.6 Tensile test measurements

TA Instruments Q800 Dynamic Mechanical Analyzer (DMA) was used to measure mechanical properties of the studied hydrogel nanocomposites. Used ramp force of 0.5 N/min at RT and at 35 % RH. Stress-strain measurements were made with a tension fixture measured as a function of several parameters: cellulose content, size and alignment of tactoids by recording stress and strain values over the measurements. Initial experiments were done on rectangular shaped specimens. This shape has however shown to be inappropriate to study our materials. For that reason, the hydrogel samples were cut into bone-like shapes using manually curved razor blades as the cutting die (Figure 15). The bone-like shape ensures that when tensile force is applied, the stress preferably concentrates in the middle of the sample. Such stress concentration results in higher probability that the sample will rupture only when reaching maximum of its possible tensile loading and the failure would occur in the narrow central region of the sample. If the specimen ruptures elsewhere (at the shoulder or right at the place of attachment), the breakage was most probably caused by an imperceptible cut of the material, which occurred during the sample attachment and the observed stress values do not necessarily represent its maximum loading possible. For that reason, all the slipped samples and the samples that broke near the clamp, are omitted from the final results.

Before each measurement, the samples were removed from water 4 minutes before the experiment to ensure well controlled equilibrium-swollen state for all of the analyzed samples.

Over this time, the dimensions (width and thickness) of the gauge part were measured and the specimens were then carefully mounted onto the apparatus attempting to avoid pre-cutting of the soft sample during the attachment into clamps. After precisely 4 minutes from removal from water medium, the specimens were subjected to a stretching force, until the material fractured. Each measurement was repeated successfully at least four times. From the stress-strain curves obtained, the stiffness of the material, ultimate tensile strength, yield strength and elongation were determined. In our experiment, mainly Young's modulus (*E*) was investigated in order to evaluate the effect of size and orientation of liquid crystals on the stiffness of the material. The numerical value *E* is determined from the early (elastic) region, where the stress is proportional to the strain and it defines the constant of proportionality, i.e., the slope of the curve. The differences in ultimate strength (the maximum possible stress before the ruptures) for different samples are also briefly discussed. However, other parameters could not be reliably determined from the measured data as the values from each experiment differ significantly due to the problems with mounting and attaching the samples.

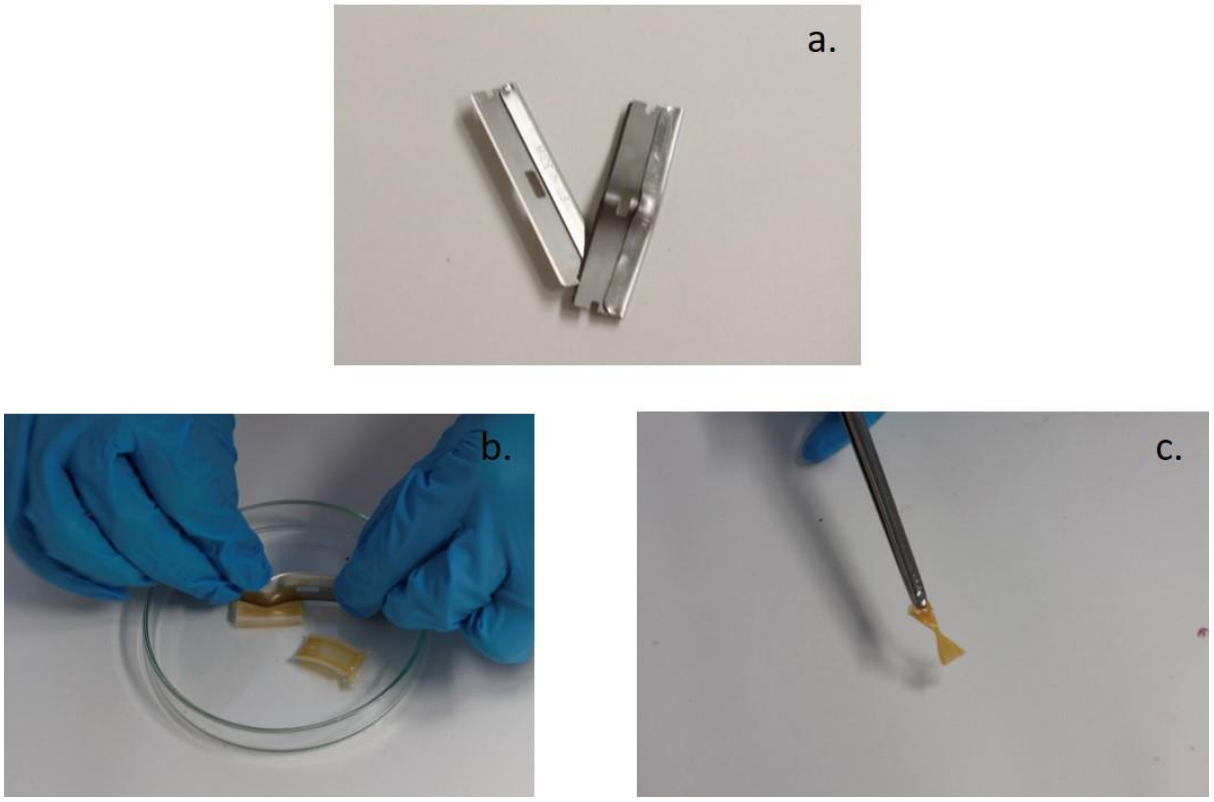

Figure 15:Specimen preparation for tensile measurements

In case of *HC$_{mg}$_4h* and *HC$_{mg}$_15h* specimens, the load was applied in the direction of the orientation of tactoids, which were embedded in the hydrogel matrix.

4.5.7 Water content

To obtain the water content of hydrogels, firstly, the weight (W_0) was measured after 4 minutes equilibration on air, in order to simulate the conditions under which the tensile strength measurements were conducted. The specimens were then placed into an oven at 40 °C. The final weight (W_x) of the dried samples was detected after 24 hours of drying. The mean free-water content ($mean_{H2O}$) for each type of sample was calculated according to the Equation 1.

$$\text{mean}_{H_2O} = \left(1 - \frac{\sum_{i=1}^{N} W_{x_i}}{\sum_{i=1}^{N} W_{0_i}}\right) * 100 \quad (1)$$

where $mean_{H2O}$ is average free-water content after 4 minutes of equilibration (%)
N is total number of measurements
W_x is final weight of the dried sample (mg)
W_0 is weight of the wet sample after 4 minutes of equilibration (mg)

And the standard deviation for each sample type was calculated using the Equation 2.

$$s = \sqrt{\frac{\sum_{i=1}^{N} \left(x_i - \text{mean}_{H_2O}\right)^2}{N - 1}} \quad (2)$$

where s is standard deviation of free-water concentration (%)
x_i is free-water content after 4 min of equilibration, sample i (mg)
$mean_{H2O}$ is average free-water content after 4 minutes of equilibration (%)
N is total number of measurements

5. Results and discussion
5.1 Characterization of cellulose nanocrystals

According to DLS, the size of the spherical particles, which have the same diffusion coefficient as CNC rods, was determined to be 164 nm. The ζ-potential of CNCs was detected to be −41 mV (Figure 16). Because the DLS measurements were repeated using the same sample several times, but the results have not changed over time and because of the high negative ζ -potential value, it was safe to conclude that the prepared CNC particles are colloidally stable.

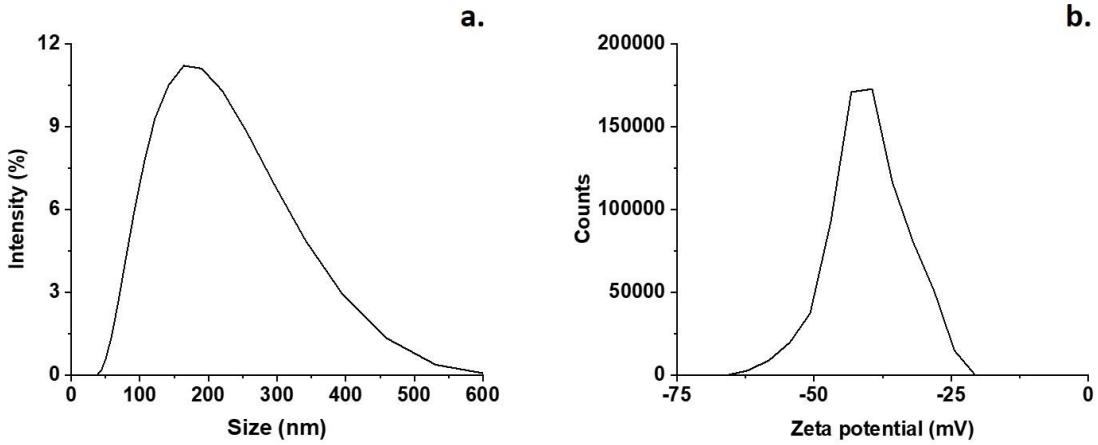

Figure 16: a) Size of a sphere that moves in the same manner as CNC;
b) Zeta potential of CNC nanorods

The TEM image in Figure 17a depicts the CNC nanorods. By conducting a TEM image analysis, the mean length and the mean width of the cotton-based CNCs was determined to be 200 nm and 40 nm (Figure 17b and Figure 17c), respectively. The measured dimensions are in accordance with the literature values for cotton-based CNCs (5-10 nm in width and 100-300 nm long).[5,96]

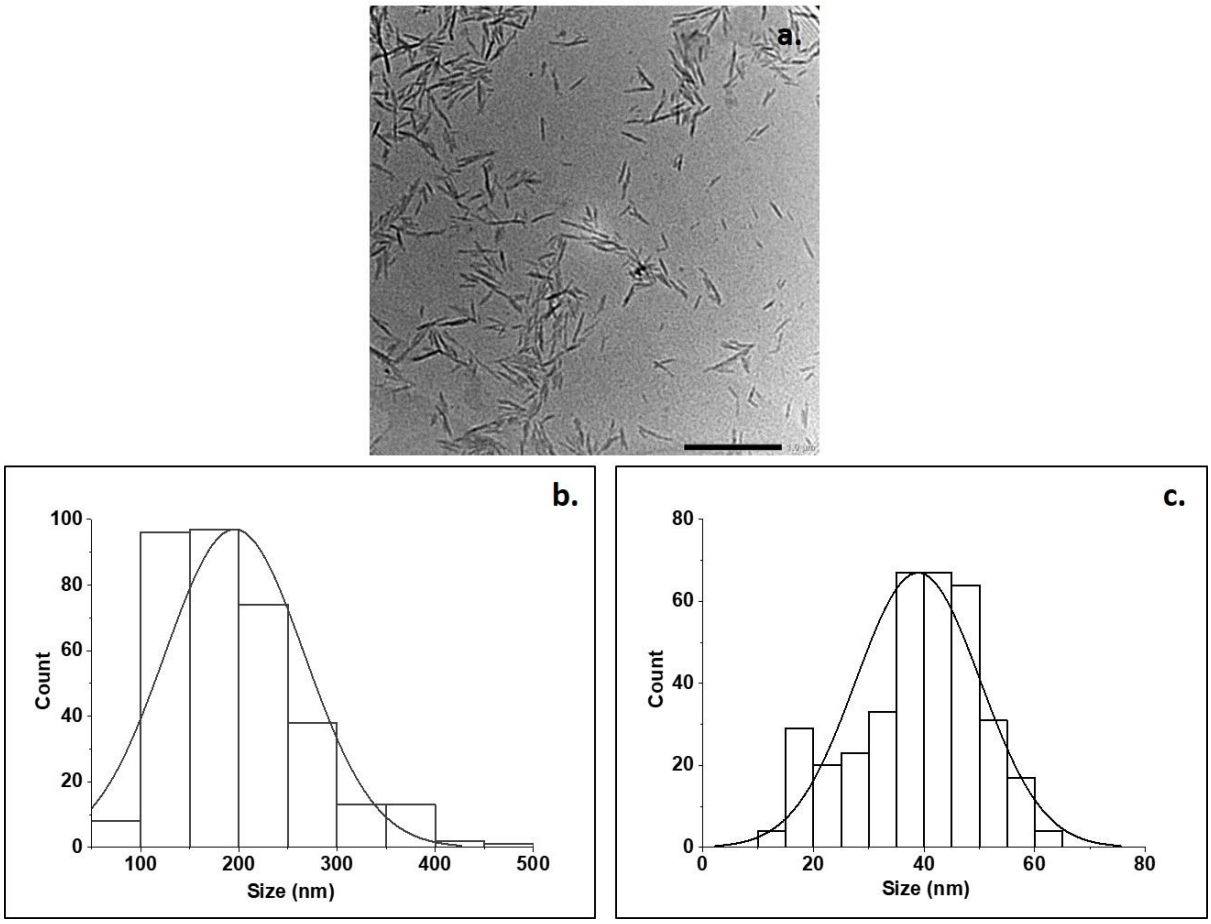

Figure 17: a) TEM image of CNCs; b) average distribution of lenghts of a CNC; c) average distribution of the widths of a CNC

5.2 Characterization of magnetic nanoparticles

According to DLS and ζ-potential measurement, the citrate-coated superparamagnetic magnetite (Fe_3O_4) nanoparticles depicted on schematic diagram in Figure 18 are around 20 nm in diameter and their ζ-potential is around -10 mV (Figure 19). Since the DLS measurements were repeated several times using the same sample, but the results did not change over time, it can be concluded that no aggregation or sedimentation has taken place and the particles are colloidally stable.

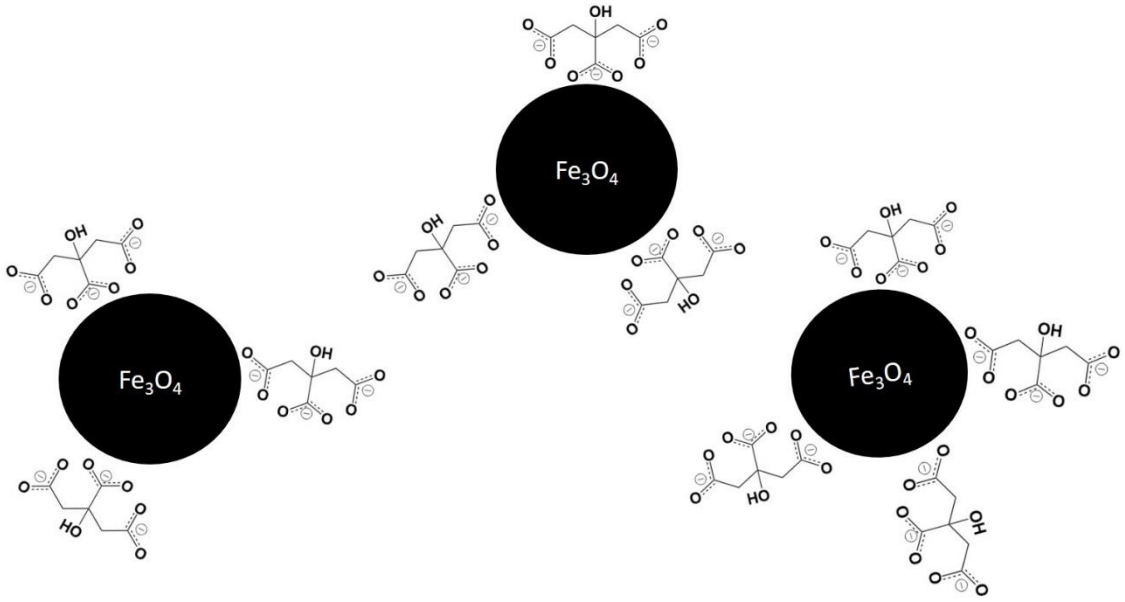

Figure 18: Citrate-coated magnetite nanoparticles

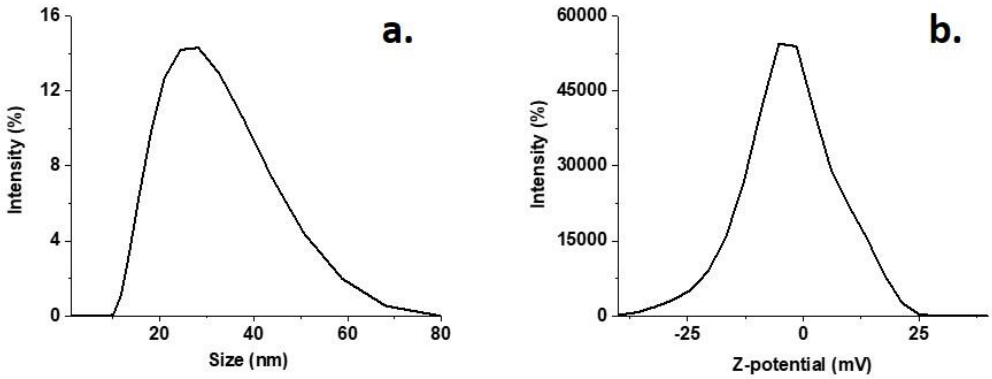

Figure 19: a) Size of the R_h of the MNP; b) Zeta-potential of the MNP

The TEM image in Figure 20a depicts the individual MNPs and no significant aggregation is observed. From TEM image analysis, the diameter of the MNP was determined to be 7 nm (Figure 20b).

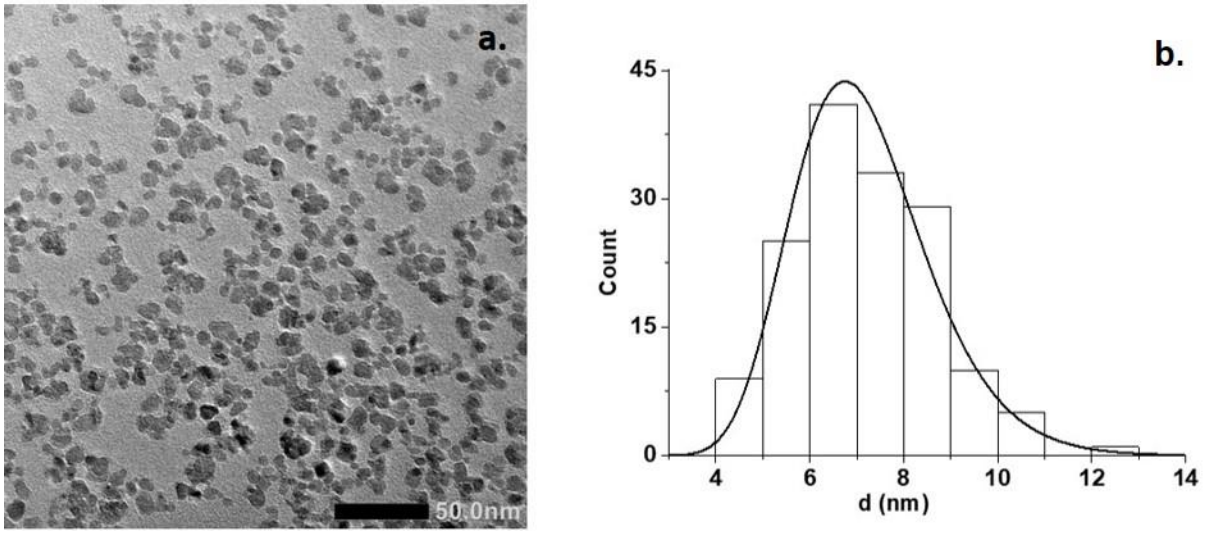

Figure 20: a) TEM image of MNPs; b) size distribution of the MNP's diameter obtained by TEM-image analysis

VSM was used to measure the magnetic properties of MNPs. This method is based on the oscillation of sample in a uniform magnetic field. The sample vibration induces voltage in the detection coils, providing information on the magnetic properties of the sample.[97] For our MNPs, the measurement provided a curve with no observable hysteresis (Figure 21). This indicates that immediately upon the removal of the external magnetic field, their average magnetization drops to zero and thus no residual magnetism remains in the particles. This is an important property of our particle, because if there was any remanent magnetization detected after removing the magnetic field, it would have caused the MNPS to aggregate.[98] The result of the VSM analysis therefore confirms that our MNPs are superparamagnetic.

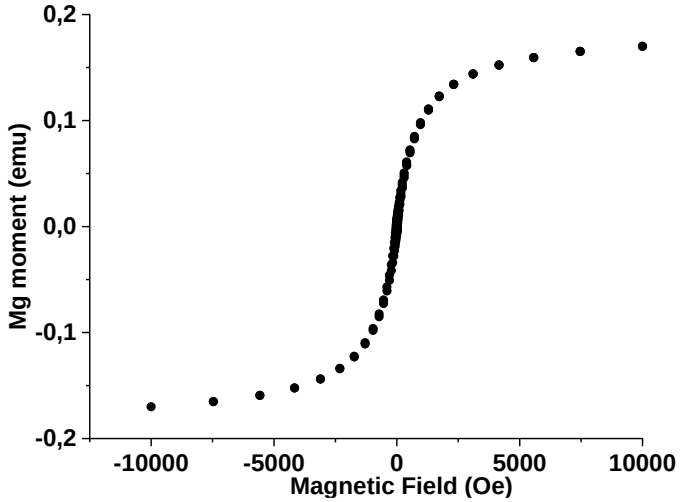

Figure 21: Magnetic hysteresis of MNP at room temperature

Furthermore, over the duration of the project, no observable sedimentation or modification of the particles was observed. Thus, we can confirm that the MNPs retained their stability.

5.3 Preliminary experiments

Firstly, the formation of chiral nematic crystalline structures from aqueous suspension, when containing sufficient amounts of CNCs, was confirmed and analyzed using POM. In general, when a liquid crystalline mesophase is analyzed by POM, the anisotropic regions show birefringence while the isotropic regions appear black under crossed polarizers. Specifically, for cholesteric liquid crystals, the growing microdomains appear as optically anisotropic ovals (tactoids), with bright birefringent bands in dark isotropic background. As the equilibration time or concentration increases, more CNCs undergo the self-assembly process, the ovals grow (increase in the number of bands), which indicates the formation of larger liquid crystals.

Figure 22 depicts the individual oval tactoids with birefringent bands. These features have formed in our CNC suspension (c_{CNC}=7.9 wt. %) after 24 hours of equilibration on a glass slide and the bands depict the characteristic fingerprint structure of cholesteric LCs of CNCs. Thus, it can be successfully confirmed, that the in-house prepared sulfuric acid-hydrolyzed CNC suspension exhibits chiral nematic liquid crystalline nature when above critical concentration.

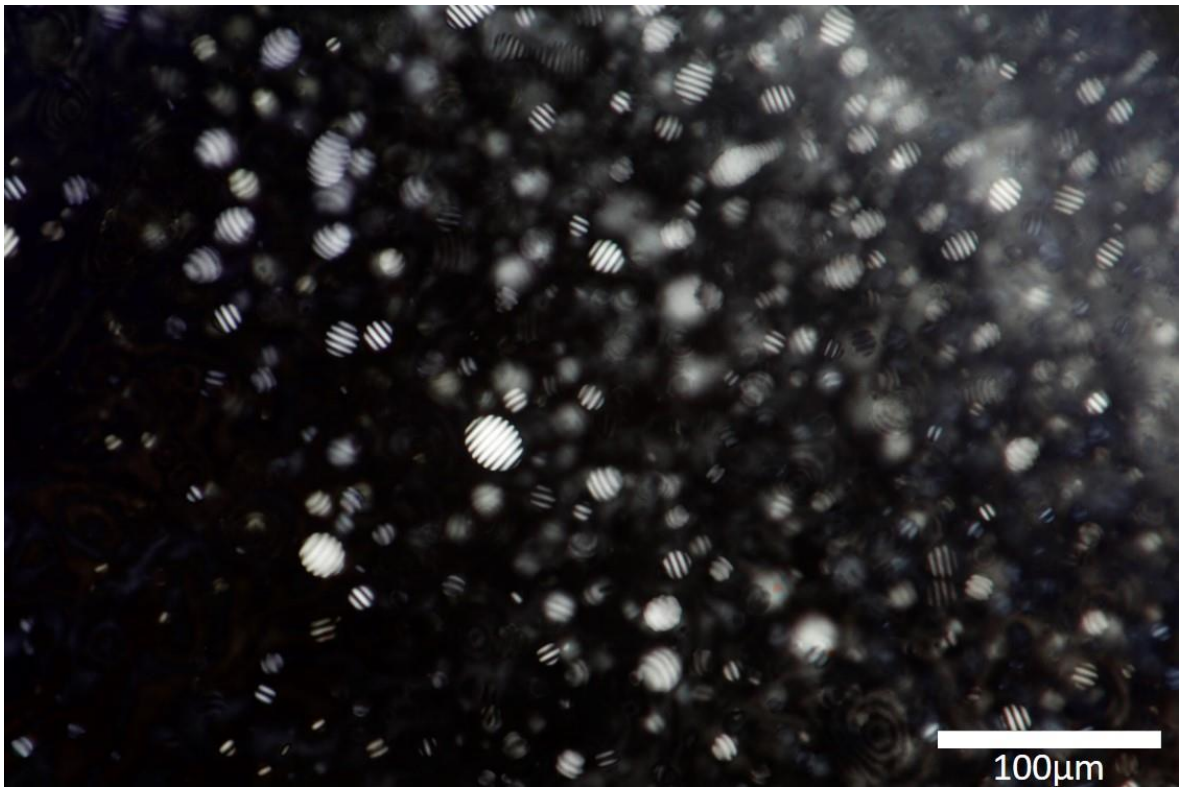

Figure 22: POM image of CNC suspension (7.9 wt. %) after 24 hours of equilibration

As mentioned previously, with longer phase-equilibration, the LCs grow in size. The liquid crystalline film depicted in Figure 23 was achieved after allowing 22 days of equilibration to a CNC aqueous suspension (c_{CNC}=7.9 wt. %).

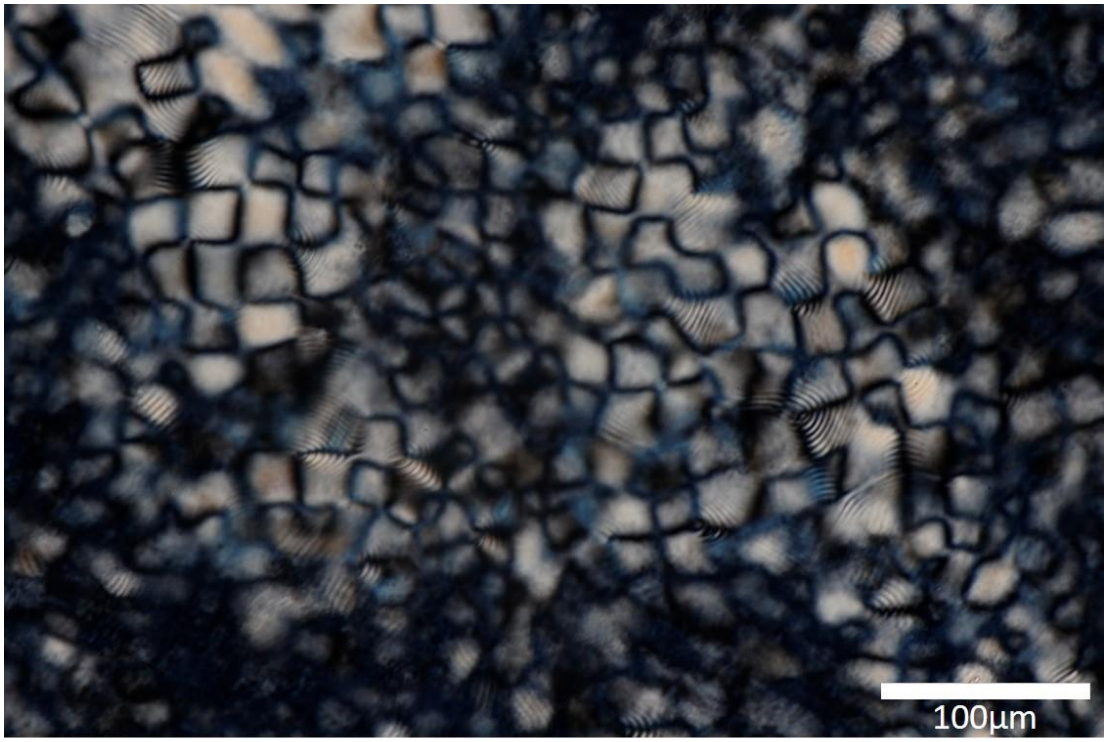

Figure 23: POM image of CNC aqueous suspension (7.9 wt. %) after 22 days of equilibration

Furthermore, it was observed that the equilibration conditions determine the tactoids' behavior. Firstly, the effect of the presence of external magnetic fields on CNC&MNP specimens (7.7 wt. % of CNCs & 2.05 wt. % of MNPs in water) was observed. As depicted in Figure 24, randomly oriented tactoids form when the aqueous solution is let to equilibrate without the presence of any external fields. However, from Figure 25, it can be concluded that when the same system is exposed to a constant magnetic field (strength ranging between 65 mT and 500 mT, see Section 4.4) over the same equilibration time, majority of the liquid crystals grow oriented along the field. The tactoids' alignment is indicated by the parallel orientation of the tactoids' bright bands, which are arranged along the direction of the external magnetic field.

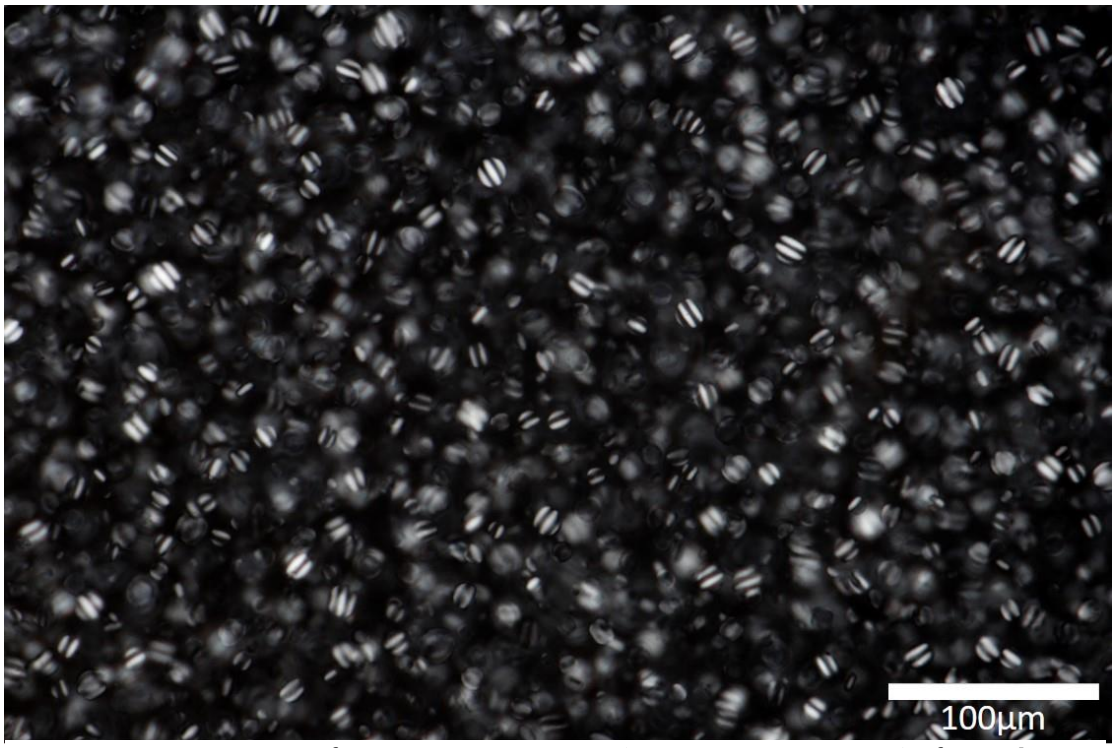

Figure 24: POM image of CNC-MNP suspension (7.7 wt. % & 2.05 wt. %) after 48 hours equilibration

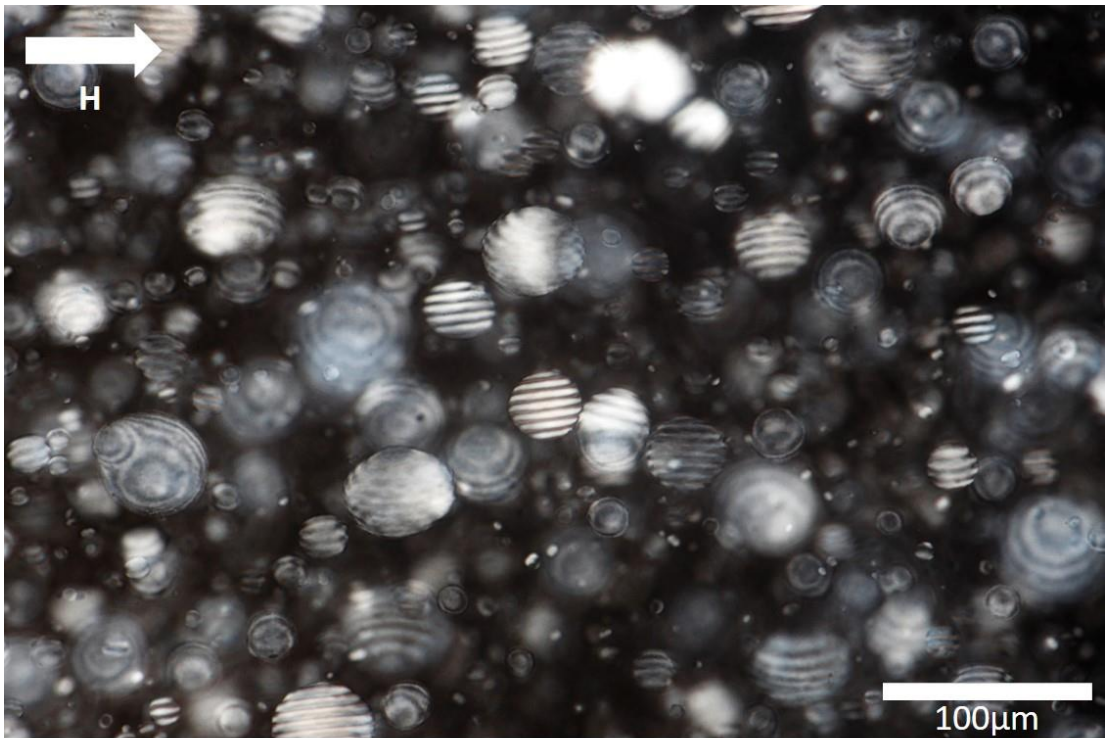

Figure 25: POM image of CNC-MNP suspension (7.7 wt. % & 2.05 wt. %) after 48 hours equilibration under a magnetic field 60-500 mT

The phenomenon of unidirectionally aligned CNC tactoids could be justified by the incorporation of MNPs within the CNC phase. This has been recently thoroughly studied by MacLachlan et al.[92], who also showed that external magnetic field drives the orientation of the CNC chiral nematic bands. The effect of magnetic field drives the dipole-dipole arrangement of the magnetic structures to form chains, meanwhile the CNCs are undergoing the self-assembly process. Since the MNPs are also present within the chiral LC regions, they inaugurate the 're-rotation' of tactoids so that the strings of MNP are well aligned along the field, causing the LCs to become aligned, too (see Figure 26). Also, by comparing the tactoids' size in Figure 25 and Figure 24, the LCs that formed in the presence of the magnetic field were significantly bigger than those that were formed freely over the same period of time. This implies, that by exposing CNC&MNP aqueous systems to magnetic fields, besides achieving unidirectional alignment of LCs, the growth is enhanced as well.

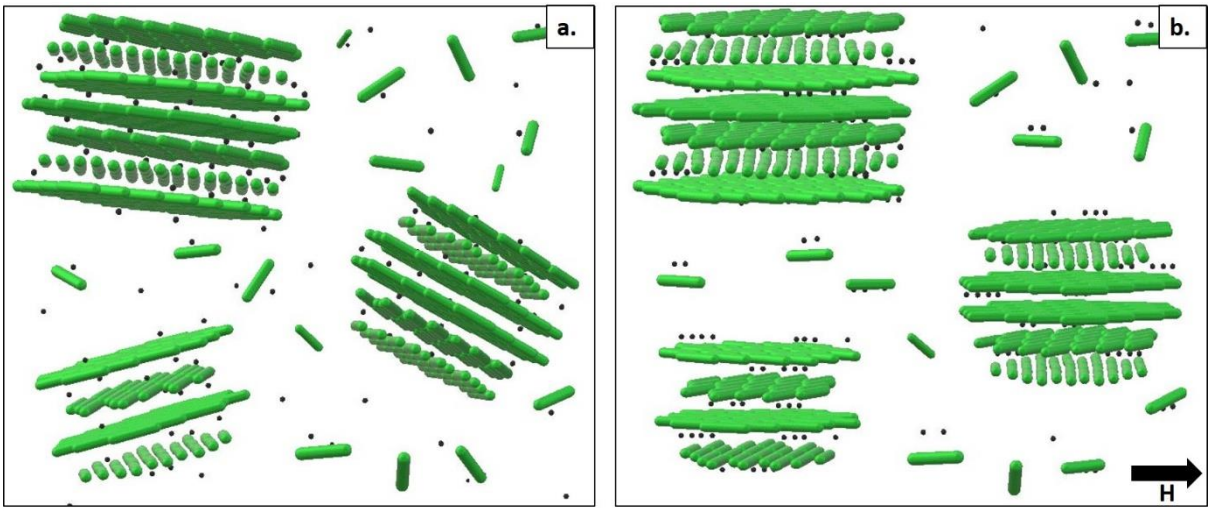

Figure 26: Scheme of CNC-MNP suspension tactoid alignment in magnetic field
a) no magnetic field allows random tactoid orientation, b) when magnetic field of the direction of the arrow, the tactoids become aligned parallel to the magnetic field due to MNP orientation effect

It is known that the anisotropic liquid crystalline phase has a higher density than the isotropic phase.[92] This behavior has also been observed in our systems. When our CNC dispersions were allowed to phase separate under static conditions, the tactoids did not remain uniformly distributed throughout the whole volume of the material. While the small nucleating LC microdomains were detected in the upper part of the material, the bigger tactoids sedimented at the bottom. And so, a 'gradient material' with a systematic LCs' size distribution was obtained. This arises from the higher density of self-assembled CNC regions and it can be explained by the effective packing of cellulose rods, in comparison to the lower density of the isotropic phase. The more CNCs are packed closely together, the heavier the phase is and the higher tendency to sediment it displays.[92] That is why the bigger tactoids are found deeper in the material, while

the smaller ones remain in the upper part. This phenomenon was quantified by POM image analysis and the collected values are depicted in Figure 27. The plot in Figure 27a shows that in the specimen, which was equilibrated for 30 minutes, the average number of birefringent bands in tactoids located at the top of the film was two bands, while the size of an average tactoid found at the bottom was 2.5 bands. Similarly, as seen in Figure 27b, after allowing the tactoids to grow over 2 hours, the top tactoids had 3.5 bands in average, while the sedimented tactoids had more than four bands.

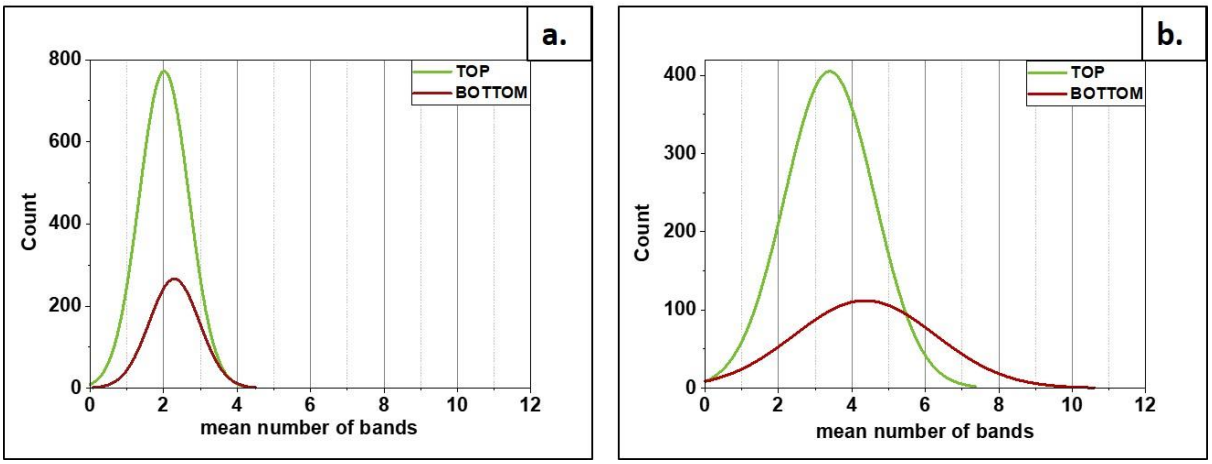

Figure 27: Comparison of tactoids' size when analyzed from top or from bottom. a) After 30 minutes of equilibration, b) After 120 min of equilibration

This analysis was done by changing the focus distance of the optical microscope. When moving the objective lens towards the film specimen, the first sharp tactoids that appeared were those small tactoids on top of the film. As the lens was positioned closer to the film, the last tactoids that were in focus, before the whole picture turned blurry, were the biggest ones at the bottom of the film.

Example of images that provided data for the plots in Figure 27 are displayed in Figure 28.

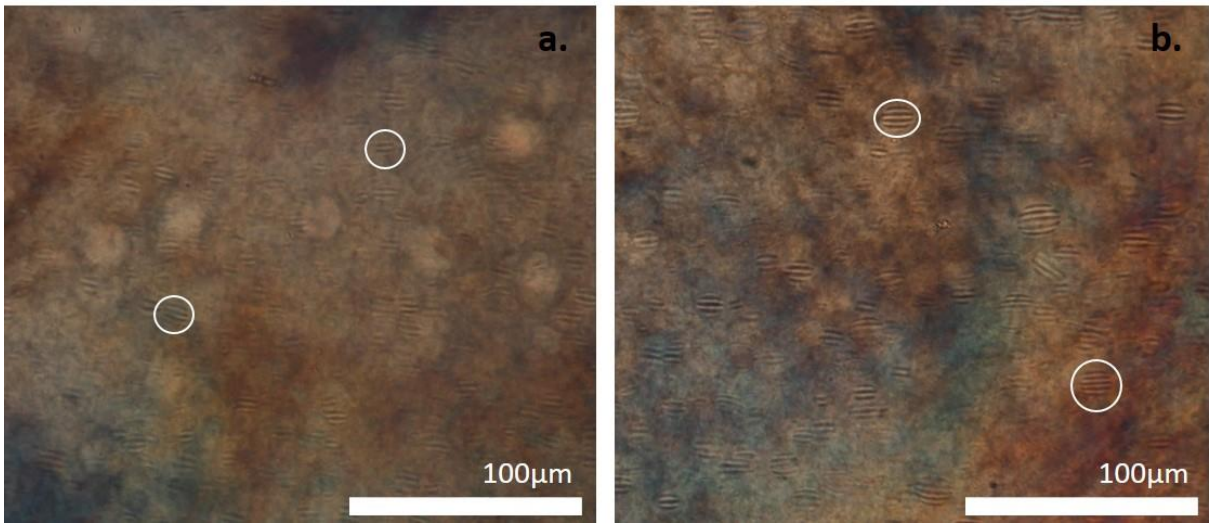

Figure 28 POM images of CNC tactoids formed in film of nanocomposite hydrogel after 120 min of equilibration on magnet and subsequent polymerization of the stock$_{HEMA}$-CNC-MNP suspension (7.6 wt. % CNC and 0.5 wt. % MNP)
a.) Observed from top, b.) Observed from bottom of the glass slide

5.4 SEM Characterization

If the CNC concentration is above the critical value and if the time allowed for phase separation (i.e. equilibration) is long enough, discrete liquid crystals trapped inside a hydrogel matrix can be observed under SEM (see Figure 29). As depicted in Figure 30, under higher resolutions, the cholesteric left-handed helical arrangement of individual CNC particles can be visualized.

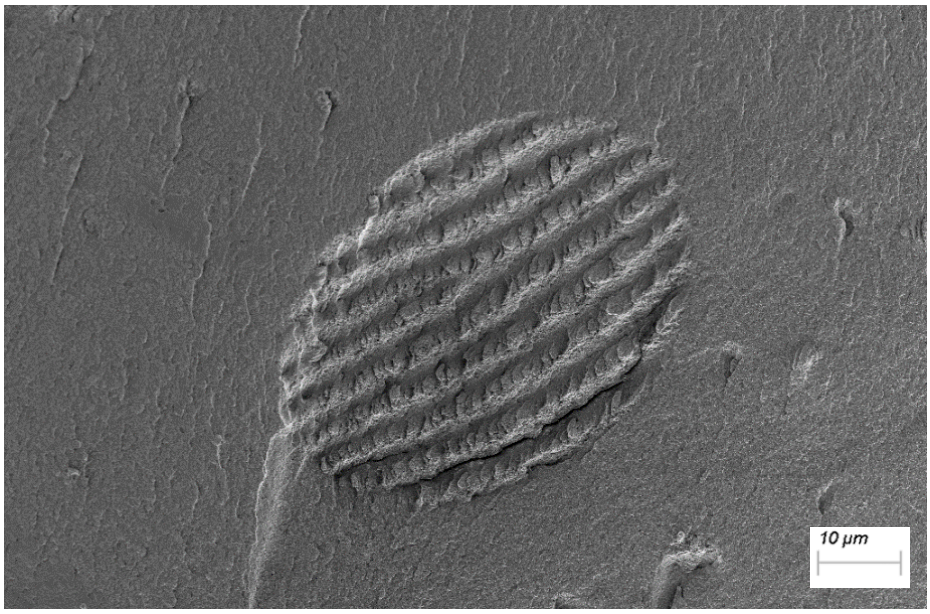

Figure 29: SEM image of a CNC tactoid doped with MNPs embedded in PHEMA matrix (7.63 wt. % CNC; 0.31 wt. % MNP) after 3 hours equilibration on magnet

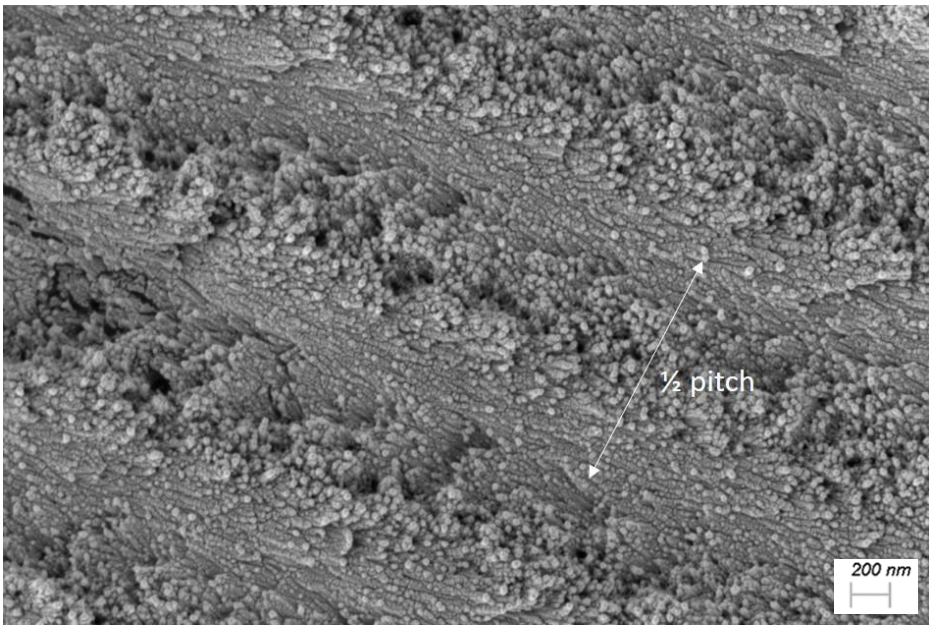

Figure 30: SEM image of individual cellulose nanocrystals in chiral nematic arrangement

When studying the morphology of our nanocomposites, the increased equilibration time allowed for the formation of bigger LC domains. This can be seen when comparing the tactoid size from *HC_4h* to *HC_15h* (Figure 31 to Figure 33, non-aligned), or HC_{mg}*_4h* to HC_{mg}*_15h* (Figure 32 to Figure 34, aligned).

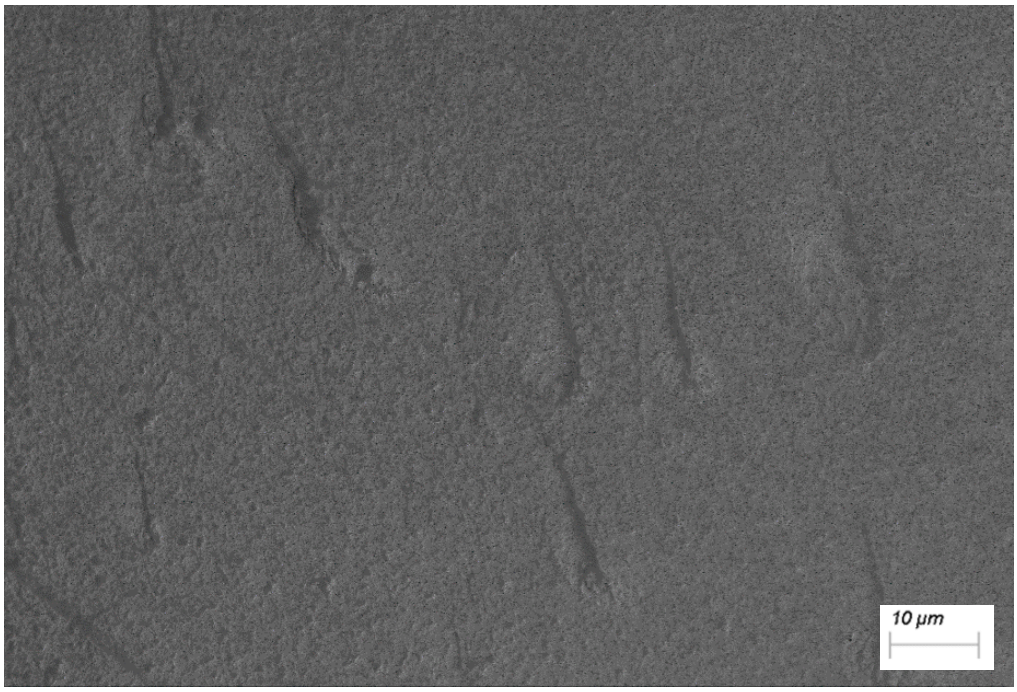

Figure 31: SEM image of tracks of unaligned CNC tactoids in HC_4h specimen

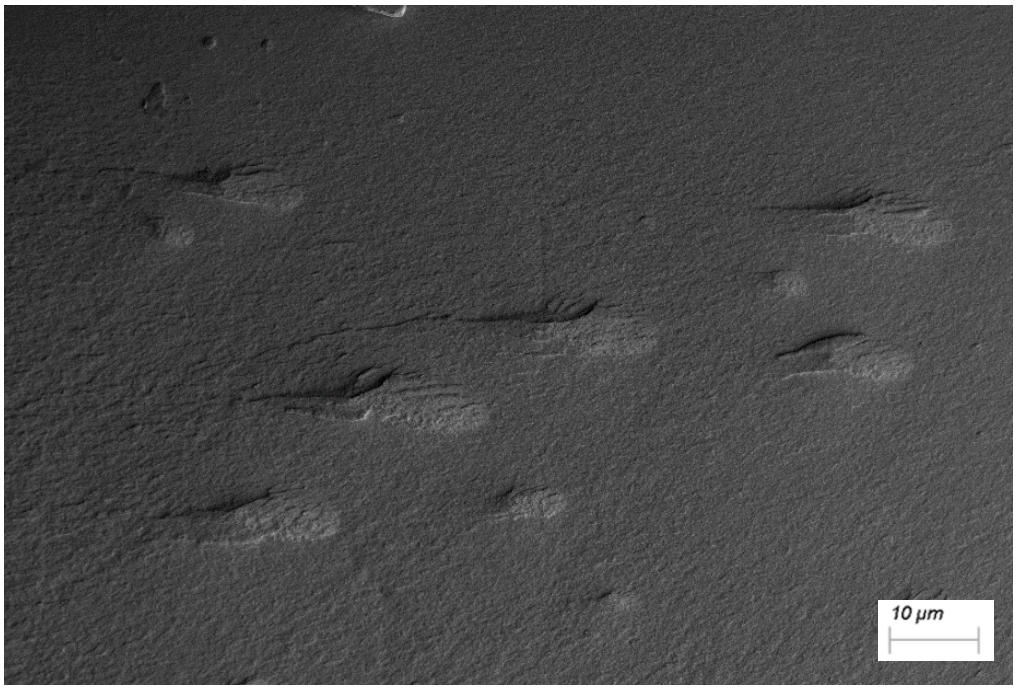

Figure 32: SEM image of aligned CNC tactoids in HC_{mg}_4h specimen

Also, it was confirmed that besides the equilibration time, also the presence of external magnetic field enhances the phase separation process. Thus, when SEM images from *HC_15h* (Figure 33) and *HC_{mg}_15h* (Figure 34) specimens are compared, not only they differ in orientation of the microdomains, but also the average size of LC domains in *HC_{mg}_15h* is bigger than in *HC_15h*.

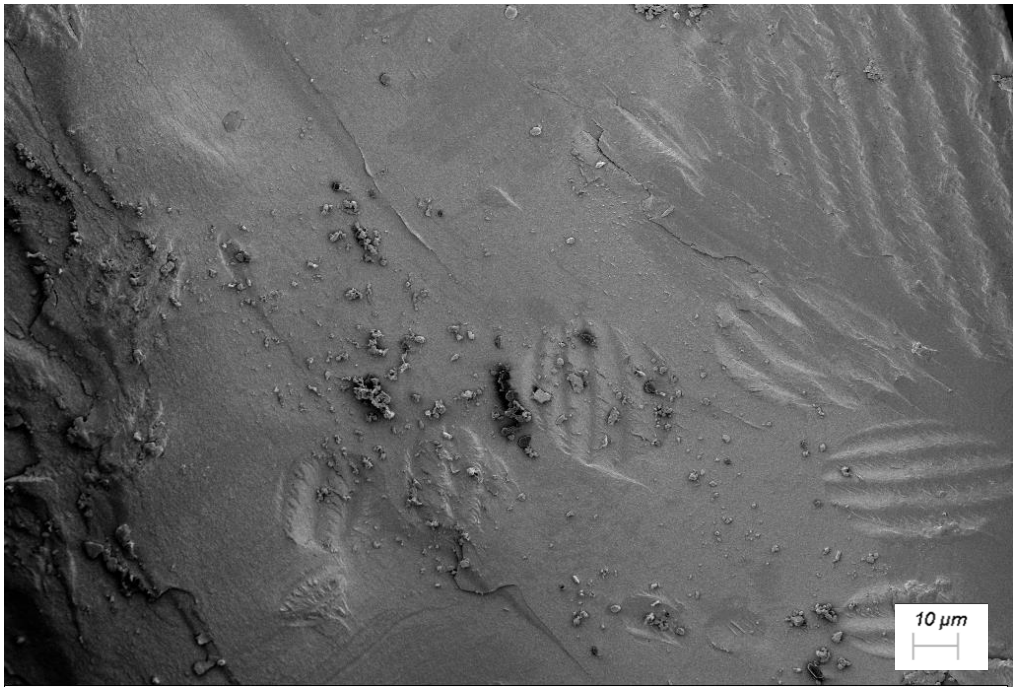

Figure 33: SEM image of unaligned CNC tactoids in HC_15h specimen

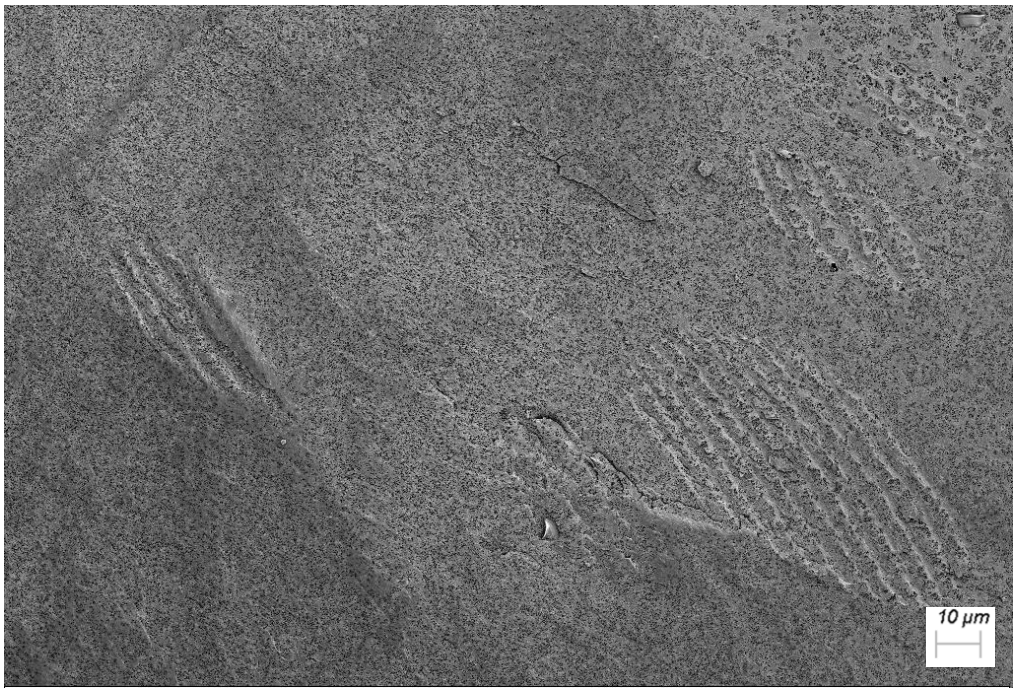

Figure 34: SEM image of aligned CNC tactoids in HC_{mg}_15h specimen

5.5 Tensile strength measurements

Initially, the tensile strength properties were analyzed on rectangular specimens by conducting uniaxial extension tests. However, all the studied samples broke at the grip and so the collected data failed to show the properties of the actual material at the maximum load. Similarly, despite the fact that great number of measurements for each batch was carried out, the results were still greatly scattered, failing to provide any reasonable conclusion on how the presence, the size, or the orientation of cellulose tactoids affects the mechanical properties of the PHEMA hydrogel.

On the other, bone-like shaped specimens showed to be more appropriate for testing because more of the analyzed samples ruptured either in the middle section, or not at the place of attachment, indicating that the stress concentration took place in the desired region. In addition, because all the measurement gave such shapes of stress-strain curve that only one tangent point is found for the secant line, it can be concluded that the samples started flowing at one specific location[99], at which the material resistance decreases so that the failure eventually takes place in this spot.

All the average stress-strain curves displayed in this section were obtained from the individual tensile tests of relevant bone-shaped hydrogel samples. All the original tensile curves, showing also the failed measurements (slipped samples and samples that broke near the clamp), are

shown in Figure 46 - Figure 51 in Appendix 1, but only the successful measurements were included in the final analysis.

First, the effect of doping PHEMA with nanocrystalline cellulose was studied. Figure 35 displays the comparison of the average stress-strain curves of *H* and *HC* specimens, PHEMA-MNP hydrogels and PHEMA-MNP-CNC hydrogels with randomly dispersed nanocrystals, respectively.

From previous studies, the incorporation of CNCs into the polymer matrix should enhance the resistance of material to external forces[100] through load-transfer mechanism between the soft and the rigid phase[87,101]. Figure 35 confirms this claim.

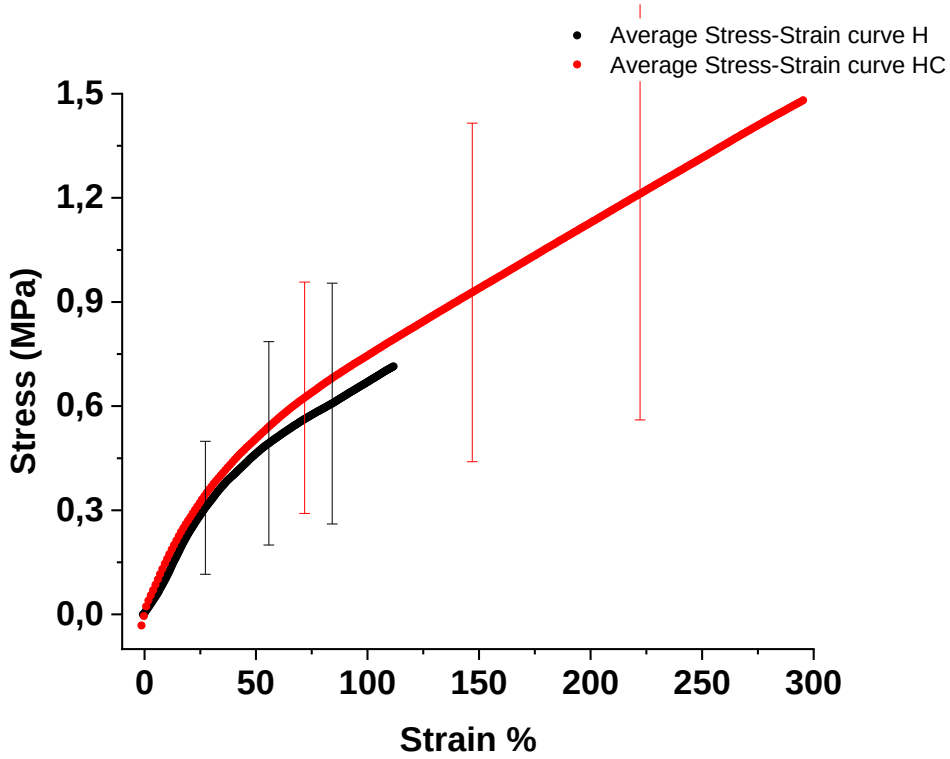

Figure 35: Average stress-strain curves for PHEMA-MNP 'H' specimens (in black) and PHEMA-MNP-CNC 'HC' specimens (in red)

Since the slope of the initial region of the *HC* curve is slightly steeper than that of *H*, it signifies that the presence of randomly distributed CNCs enhances the stiffness of the material, i.e. increase in Young's modulus, resulting from the phenomena of mechanical percolation.[46,47] Also, the ultimate strength of the cellulose nanocomposite material *HC* appears to be more than double in comparison to pure PHEMA, *H* specimen. Yet, this observation is not necessarily reliable as the variability of the collected data is significant. The comparison of the Young's moduli and Ultimate Strengths are depicted in Figure 36 and in Figure 37, respectively.

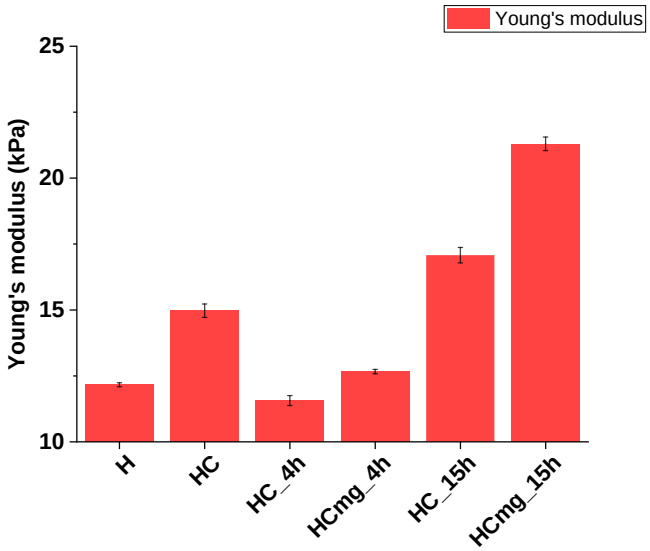

Figure 36: Average Young's modulus for each type of hydrogel nanocomposite

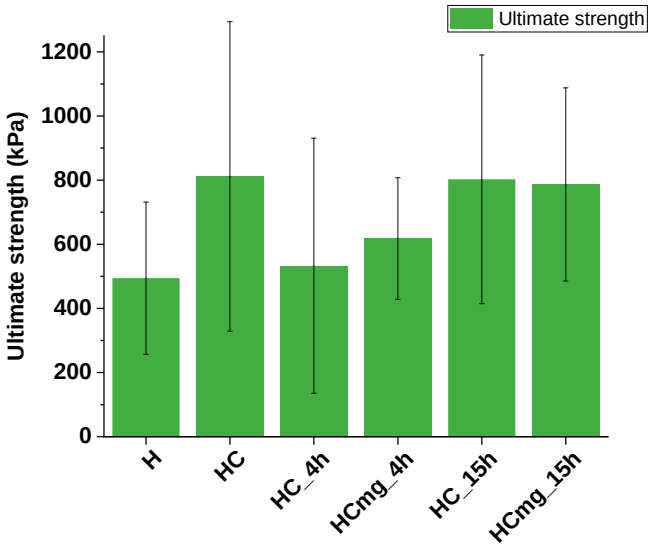

Figure 37: Average Ultimate strength for each type of hydrogel nanocomposite

The numerical values of the average Young's moduli, the average ultimate strengths of the analyzed specimens and the corresponding standard deviation values are summarized in Table 3 and in Table 4, Appendix 1.

In case of nanocomposites, the applied load is shared between the weak matrix phase and the reinforcements.[87] In our system, the reinforcement structures are represented either by individual CNCs (*HC*), or by cholesteric microdomains of LCs (*HC$_{(mg.)}$_4/15h*), both distributed in the volume of the softer PHEMA matrix. The load-bearing ability of the reinforcing phase is determined not only by its type and volume fraction, but also by its size, shape and orientation.[87] Thus, prior to the experiments, it was expected that the 4-hours equilibrated/aligned hydrogels would show enhanced mechanical behavior in comparison to *HC* and *H* hydrogels. This is due to the layered structures of CNC's LCs, which are not only bigger than the individual rods, but also hierarchically organized.

However, on the contrary, the mechanical properties of *HC$_{mg}$_4h* and *HC_4h* specimens have shown to be weaker than *HC*, or at best similar to the *H* hydrogels (see Figure 38).

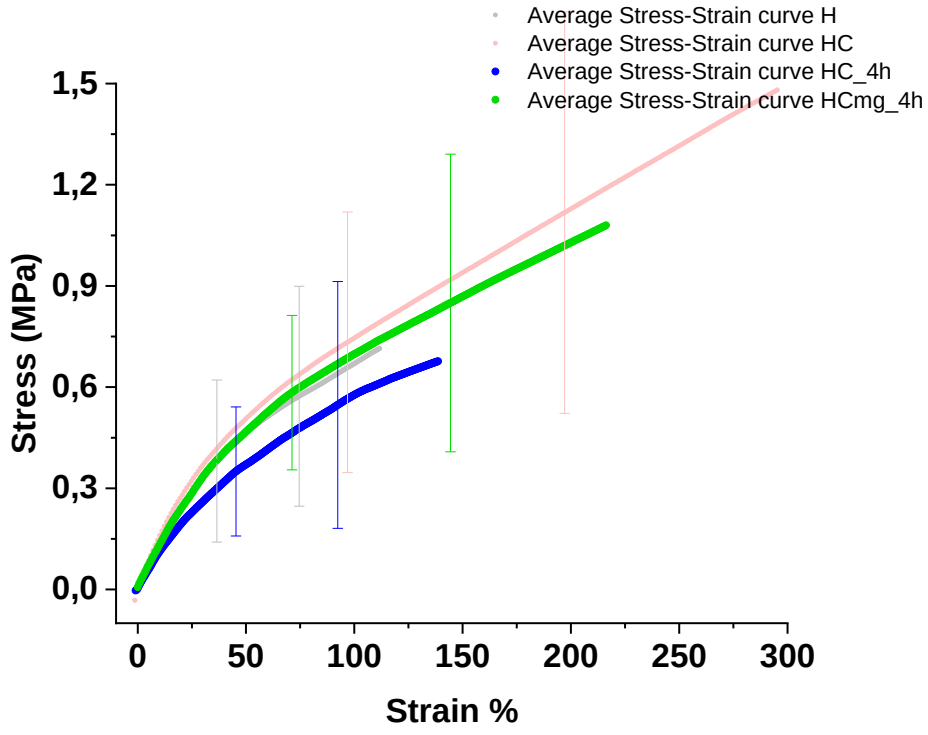

Figure 38: Average stress-strain curves for PHEMA-MNP-CNC 'HC$_{mg}$_4h'(in green) in comparison to 'HC_4h' (in blue), 'HC' (in light red) and PHEMA-MNP 'H' specimens (in grey)

Even though the *HC$_{mg}$_4h* specimens comprised of cholesteric microdomains, that were formed by the self-assembly process of CNCs over 4 hours, were rather small and so they did not contribute to the material's resistance to external forces. When the Young's modulus of these 4 hours-equilibrated samples was compared to that of *HC* (see Figure 36), it actually showed decline in the load resistance. This observation can be explained by the fact, that portion of the initially randomly distributed rigid CNCs starts to cluster into small organized domains, 'consuming' the particles and leaving the rest of the volume lacking the reinforcement

structures. Since the formed tactoids are responsible for the partial depletion of CNCs and their size appears to be insufficient to exhibit reinforcing effect, the stiffness of *HC_4h* nanocomposites shows to be analogous to the *H* hydrogels, which consist of PHEMA-MNP only. In *HC$_{mg}$_4h* specimens, the deficiency in reinforcing rods is somewhat compensated by the tactoids' alignment along one direction, leading to the enhancement of material anisotropy, which results in increased stiffness when load is applied in the direction of the alignment.

The comparable values of ultimate strength of *H* and *HC_4h*, depicted in Figure 37, may be explained by their structural similarity, having the majority of the specimen lacking the presence of the reinforcing CNC particles. For *HC$_{mg}$_4h*, even though that the aligned tactoids improve its stiffness, once the film starts to deform plastically, the small liquid crystals are no longer able to prevent the fracture. Therefore, this type of hydrogels ruptures sooner than the *HC* films, which contain randomly distributed CNC throughout their whole volume. Furthermore, it was also expected that with the increased size of CNC liquid crystals, the stiffness of the nanocomposite would be enhanced, since it is expected that bigger rigid LC microdomains are more resistant to the applied load.[101] Also, as mentioned earlier, the alignment is expected to play important role in composite's mechanical performance.

The considerably bigger size of tactoids in the *HC$_{mg}$_15h* films indeed gave rise to stiffer materials. This can be observed both, from the slope of the curve in the linear elastic region in Figure 39 and also from Figure 36 (E = 21.3 kPa, Table 3 in Appendix 1).

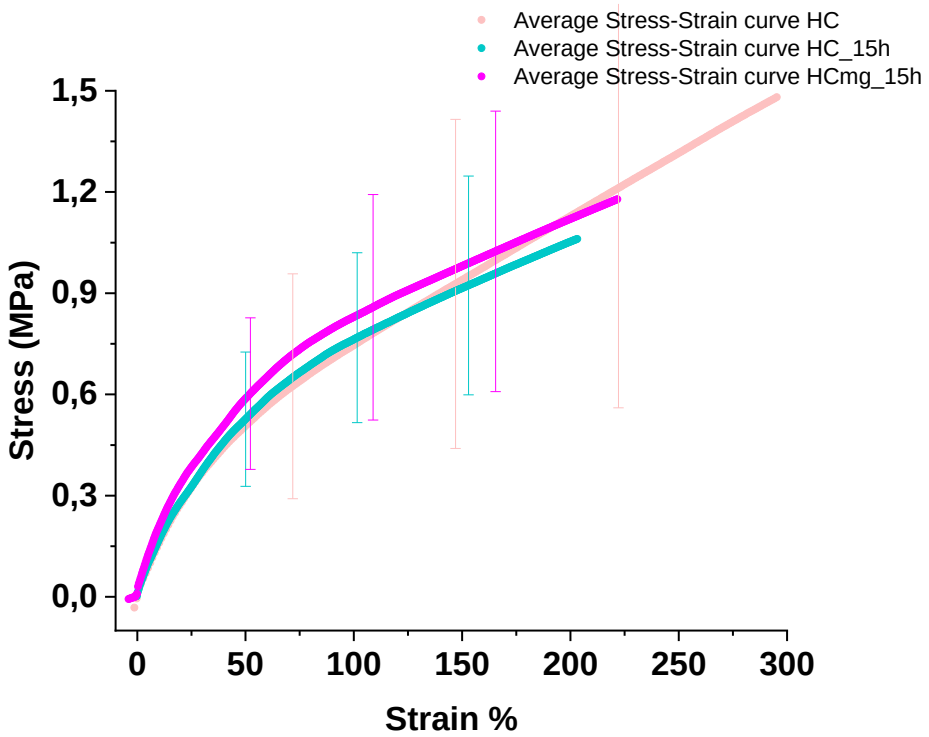

Figure 39: Average stress-strain curves for PHEMA-MNP-CNC 'HCmg_15h' (pink), 'HC_15h' (turquoise) and 'HC' (light orange),

This mechanical enhancement can be explained by the synergy between the intrinsic mechanical properties of individual CNC rods and the hierarchically organized CNC tactoids of unidirectionally layered nanocrystals, which are similar to the structure of platelet-reinforced polymer films.[101]

Bonderer et al.[101] have suggested that there is a size limit for reinforcing structures to exhibit enhancing effect. It is assumed that when the limit is exceeded, instead of achieving a material of extraordinary stiffness, the material would begin to exhibit brittle fracture under tensions because of its flaw intolerance. The size limit of cellulose tactoids has not been studied, yet. Therefore, it could the subject of research in another project.

Finally, also the effect of uniform alignment of liquid crystalline regions was studied. From Figure 40, the tensile measurements of both *HC$_{mg}$_4h* and *HC$_{mg}$_15h* showed higher stress yields than their respective unaligned samples, though the difference between *HC_15h* and *HC$_{mg}$_15h* specimens was not too significant.

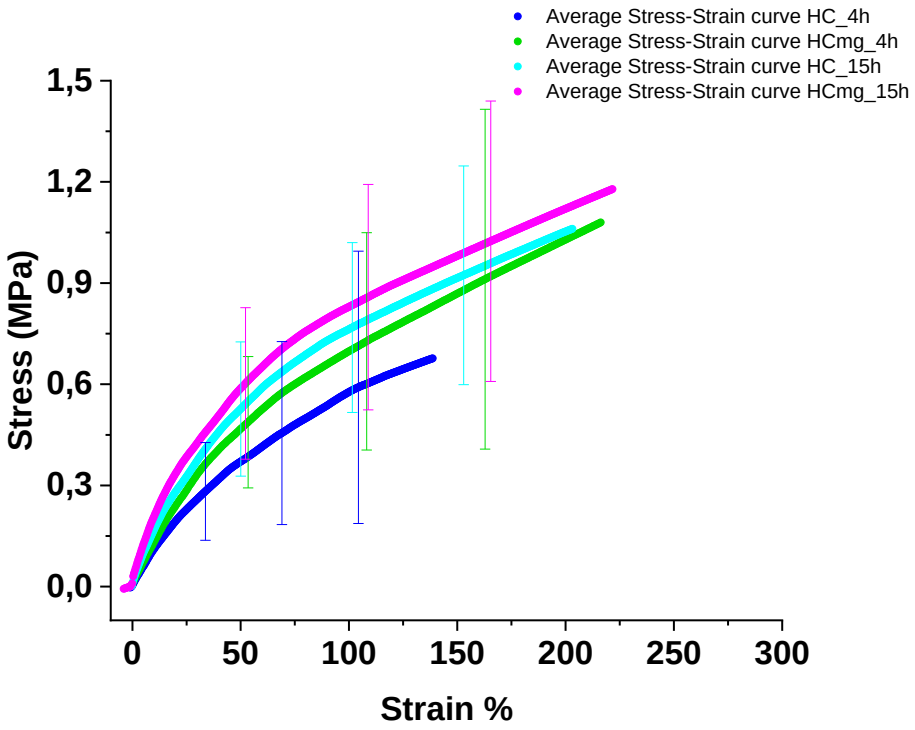

Figure 40: Average stress-strain curves for PHEMA-MNP-CNC 'HC$_{mg}$_4h' (in green) and 'HC$_{mg}$_15h' (pink), in comparison to 'HC_4h' (in blue) and 'HC_15h' (cyan)

Similarly, the average Young's modulus of hydrogels with unidirectionally aligned tactoids is higher (see Figure *36*) (E_{HCmg_15h} = 21.3 kPa and E_{HCmg_4h} = 12.7 kPa from Table 3 in Appendix 1) with respect to those that are randomly oriented (E_{HC_15h} = 17.1 kPa and E_{HC_4h} = 11.6 kPa). This finding supports our assessment, that when the reinforcing microstructures are aligned along a common direction, the material exhibits higher endurance towards external unidirectional stresses. This can be linked to the fact, that defects are prevented from proceeding fast across the sample diameter perpendicular to the alignment. In addition, the synergy effects of the dispersed aligned microdomains, which are randomly distributed throughout the volume (if neglecting the gradient distribution due to sedimentation of bigger LCs), also play role in the materials' mechanical properties.

Figure 41 depicts all the average stress-strain curves characteristic for each type of analyzed nanocomposite material. From the profile of the curves of various samples are comparable and all the hydrogels (only after 4 minutes of equilibrating on air) were soft and flexible materials.

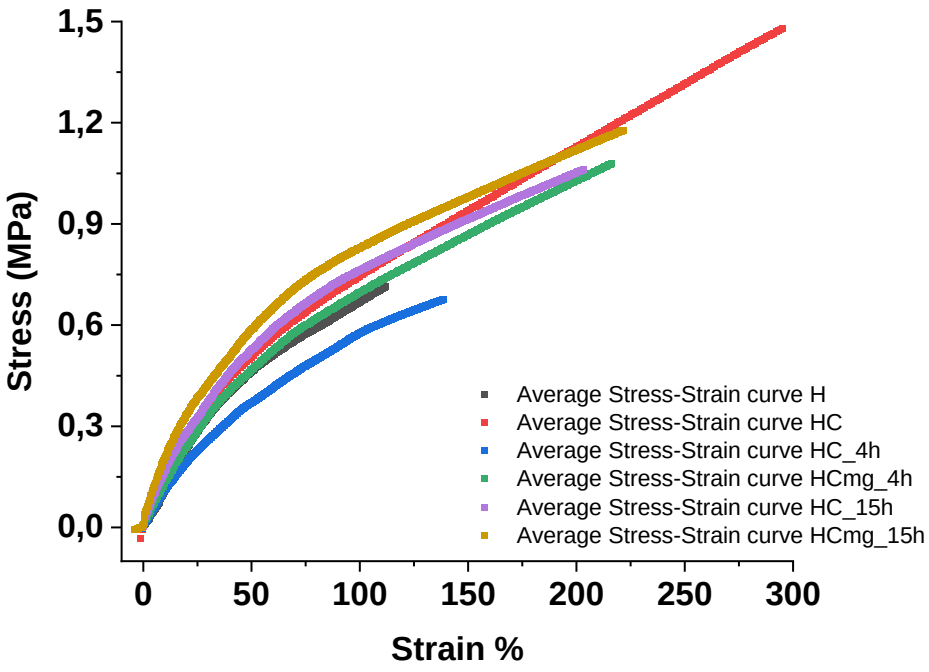

Figure 41: Average stress-strain curves for all studied hydrogel nanocomposites

Even though the average Young's moduli and Ultimate strength values are improved for hydrogels with bigger and aligned CNC tactoids, they are still roughly of the same order of magnitude for all the studied nanocomposite films (see Figure 36 and Figure 37). Thus, the enhancement of the mechanical performance has not been as significant as anticipated. What should be also noted, is that the accuracy of the ultimate strength values is questionable due to considerable variations in the individual measurements (significant standard deviation values).

It can be also noted, that when longer time on air was allowed for the hydrogels before conducting the tensile experiments, they quickly dried out and turned into hard, brittle material. Such specimens were impossible to analyze under given conditions due to their breakage during the mounting process or slippage from the grip of the apparatus during the measurement.

The displayed average curves were obtained from the individual tensile tests of relevant types of hydrogel samples. All the original tensile-test, showing also the failed measurements that were excluded from the analysis, are shown in Figure 46 - Figure 51 in Appendix 1.

5.6 Possible sources of errors

The standard deviation values of ultimate tensile strength of the analyzed materials are undesirably high. Also, the individual stress-strain curves showed considerable scattering (see Figure 46 - Figure 51 in Appendix 1). Such unsatisfactory data can be caused by various factors.

Firstly, the preparation procedure of the samples was not perfectly optimized as alternative tools (glass quartz cuvette sealed with Teflon tape and closed with lid of the same material, handcrafted cutting die) were used to prepare suitably shaped specimens. Since the cutting was done without any template, the individual specimens varied in dimensions. The small differences in sizes could lead to unequal water content during the testing, as the water-equilibration time was kept at 4 minutes for all samples, regardless their size. In addition, since the hydrogels still contained water and no chamber was used to control the water content over the measurement process, the samples continued drying. This decrease in water content inevitably resulted in small changes in dimensions even over the time of their stretching. This is a common problem encountered when analyzing hydrogel samples.

Moreover, due to the specimens' nature, certain obstacles were encountered over the execution of tensile measurements. When samples were handled imprudently, the soft notch-sensitive material was pre-cut. This took place for instance when the samples were mounted onto the apparatus, or during the attachment into the metal grips. When such defect was detected (for instance when bone-shaped sample ruptured at the place of attachment), the corresponding data was excluded from the final results. Also, those specimens, that clearly underwent slippage, were not included in the final results. Yet, it is possible that some unrevealed slip took place, which would contribute to the variations in the collected data. Further, as mentioned in Section 5.3, an unintended gradient in the tactoids' size distribution was obtained, resulting from the differences in the density of the phases.

Additionally, in the samples that were exposed to magnetic field, a certain degree of aggregation of the MNPs was observed (Figure 42). This clustering process was detected at the ends of the films, which correlates to the inhomogeneity of the strength of the magnetic field generated by the permanent magnet (see Figure 14 in Section 4.4).

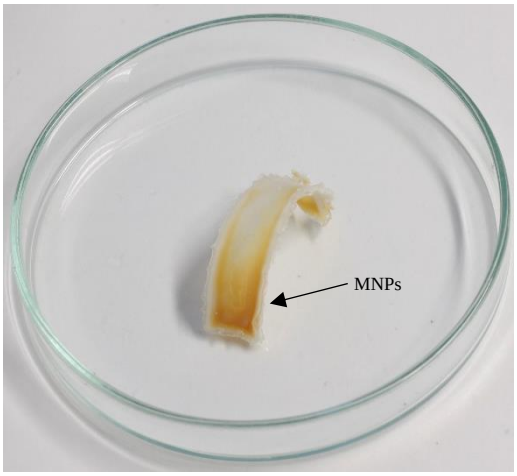

Figure 42: Aggregation of MNPs on the edges of the HCmg_15h specimen

5.7 Water content measurement

Figure 43 indicates the weight content of water in the studied hydrogels after 4 minutes of equilibration on air (to model the conditions of tensile measurements). From the obtained data (considering the standard deviation values), the water content does not significantly differ for different hydrogels. In all the CNC-containing samples (all besides *H* specimens), the water content of the polymerization mixture (orange line) corresponds to the measured water content. This means that no solvent becomes irreversibly incorporated in the matrix and the water used as solvent accumulates in pores. Also, this it indicates that no significant absorption takes place, despite storing the hydrogels in water for several days. For *HC* and *HC_15h*, the water content is slightly higher than the amounts used for the reaction. This is probably due to the storage conditions of the samples (stored in water) as small additional amounts of water could enter the pores. For HC_{mg}*_4h* specimens, the higher value may be either due to storage conditions, plus accidently using a wet flask for mixing the solution, or another explanation may be a systematic error in measuring the weight of the specimens. Yet, no observable swelling upon storage in water was detected.

In the case of *H* specimens, the amount of water used as solvent in the polymerization was higher by 8 wt. % (i.e. 59.31 wt. %, see Table 2 in Section 4.4 showing reactants concentrations). That is why the reference orange line is placed higher for *H* hydrogels. The

difference between the measured water content (i.e. the evaporated water) and the initial water content of polymerization mixture of *H* hydrogels suggests that some of the solvent-water becomes bound to the hydrophilic groups in the matrix and therefore is not removed by evaporation.[67] For that reason, the amount of 49.1 wt. % in *H* samples can be denoted as free-water, because it was evaporated. The remaining 10.21 wt. % was retained in the *H* hydrogels.

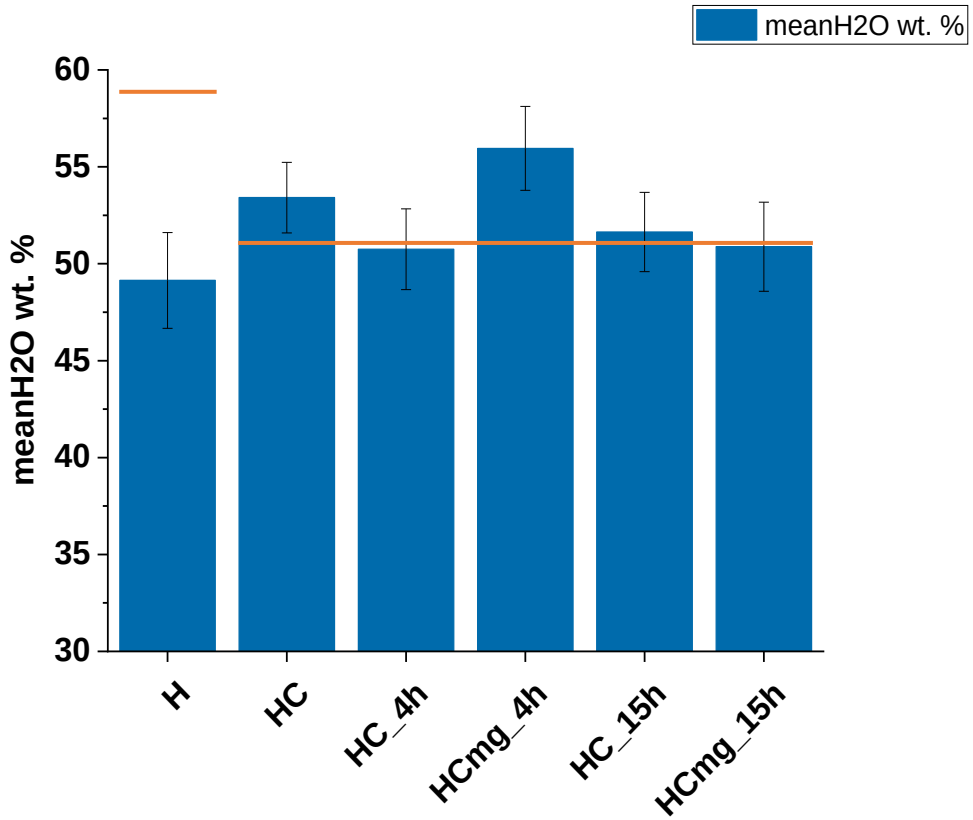

Figure 43: Free-water content of H specimen (PHEMA-MNP) and of other hydrogels HC$_{(mg)}$_Xh (PHEMA-MNP-CNC) after 4 minutes of equilibration on air

According to Figure 43, *H* samples show more or less the same water content like the other specimens. This indicates that if higher amounts of water were used in the polymerization mixtures of other CNC-containing samples too, the final nanocomposites would retain some water. Maximum water that can be bound by the matrix was calculated according to the Equation 3, using the values of *H* sample.

$$H_2O_{bound\ max} = \frac{59.3-49.1}{59.3} * 100\% = 17.2\ \% \qquad (3)$$

The numerical values of water in the analyzed specimens and the corresponding standard deviations are summarized in Table 5 in Appendix 1. All the hydrogels were stored in water, but no detectable additional water uptake (i.e. no increase in weight or swelling) was detected. Figure 44 shows that wet hydrogels were rather translucent and not fully transparent. On the other hand, Figure 45 depicts the increased transparency of the same, but dried, specimen. This

behavior was discussed by Gulsen and Chauhan[102] who suggested that when water is inside the pores, they are bigger, which reduces the transparency, leading to opaque material. While in dry hydrogels, the pores are so small that the light can pass through the material without any strong reflection.

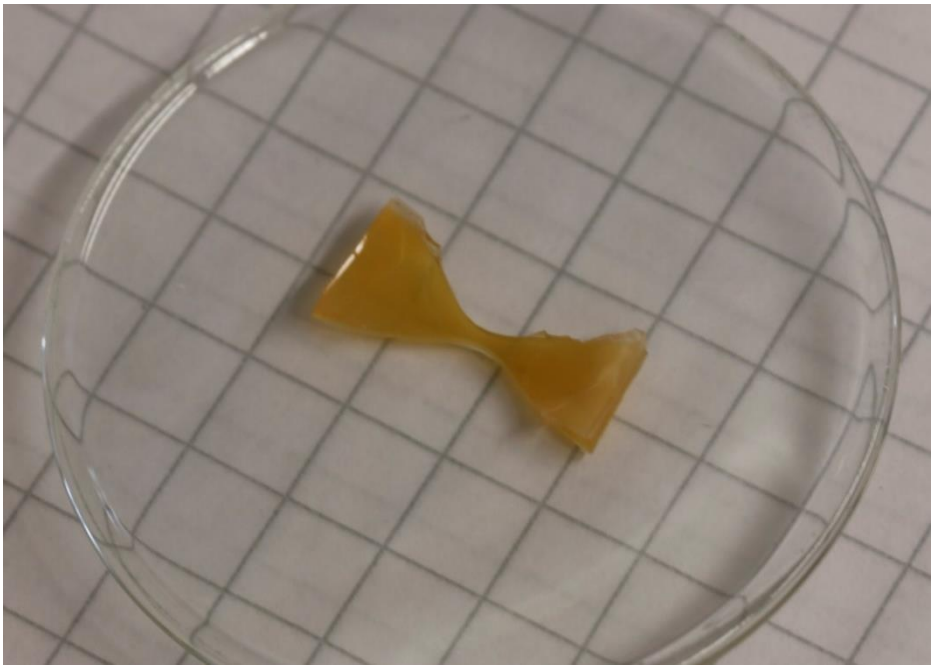

Figure 44: Wet translucent HC hydrogel nanocomposite

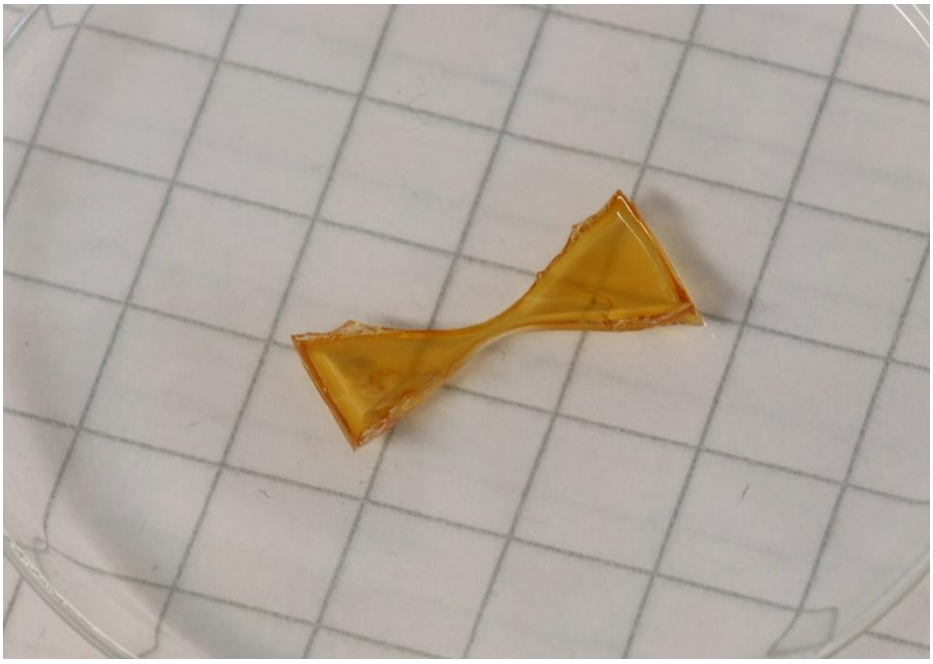

Figure 45: Dry transparent HC hydrogel nanocomposite

6. Conclusions and outlook

Novel nanocrystalline cellulose-based hydrogels were successfully designed in this project. Firstly, it was achieved to embed individual CNC rods in PHEMA hydrogel. This showed, that the dispersed CNCs provide reinforcement for PHEMA hydrogels, similar to the effect of reinforcement of methacrylate hydrogels by bacterial cellulose published by Hobzova et al.[100]. Secondly, the self-assembly behavior of CNCs was exploited. By allowing reasonable times for phase-separation, cellulose liquid crystalline tactoids formed in the polymerization solution. They were then successfully locked in the PHEMA matrix by UV-induced polymerization. Additionally, the liquid crystals' size was determined by the phase-equilibration times. Moreover, by incorporating superparamagnetic nanoparticles into the system, we accomplished to control the orientation of cellulose liquid crystals by applying only small DC magnetic fields. Even though we faced some difficulties with tensile measurements and despite the fact that the quality of the data failed to meet our expectations, the measurements provided promising trends. The data showed that the enhancement of the mechanical behavior strongly depends on the size and on the orientation of the reinforcing microdomains. It was found out, that only sufficiently big liquid crystalline tactoids lead to the improvement of the material behavior. This can be explained by the synergistic effect between the individual CNCs and their hierarchical liquid crystalline arrangement. Moreover, the distribution of tactoids was not uniform throughout the volume of the material. As the liquid crystals grew in size, their density increased, so they had higher tendency to sediment at the bottom. This finding could be interesting for further studies, which could lead to the development of new materials with gradient structures.

In future, if the experimental parameters are carefully selected and phase behavior of all components is considered, a new non-gradient material with uniformly distributed stiff microdomains could be developed. Similar concepts have been previously studied on other complex systems.[103,104] Also, further optimization of the preparation conditions, such as uniform magnetic field, suitable mold and better die cutter tools, are crucial for obtaining more consistent and precise data.

In order to provide a more general outlook, the concept of CNC-based cholesteric liquid crystals and hydrogels suggests interesting research potential. The combination of ferromagnetic nanoparticles (ferrofluids) and cholesteric liquid crystals, was suggested already in 1970 by Brochard F. and De Gennes P. G.[105], who predicted complex phase behavior of such systems. Thereafter, considerable literature on molecular level cholesteric liquid crystals combined with

magnetic nanoparticles was published.[106] But, as it was shown in this work, to achieve stable one-phase material without phase separation of the lyotropic liquid crystal and the magnetic nanoparticle can become subtle. For instance Ménager et al.[107] showed that surfactant based lamellar phases and magnetic nanoparticles can co-exist in a single phase if the concentrations are low, still extremely carefully chosen. This suggests that also in the case of our system, in future, we should pay greater attention to the nanoparticle concentrations. In overall, CNC-based ferrocholesterics seems to be little studied, nevertheless very unprecedented findings on these system have been done, such as that ferrocholesterics based on the molecular level liquid crystals allow for topological structures, like skyrmions.[108] Based on these arguments, systems comprising of CNCs, with their inherently large dipole moments, and magnetic nanoparticles embedded in deformable hydrogels suggest interesting research possibilities for complex responsive materials.

7. Bibliography

1. Wegst, U. G. K., Bai, H., Saiz, E., Tomsia, A. P. & Ritchie, R. O. Bioinspired structural materials. *Nat. Mater.* **14**, 23–36 (2015).
2. Fengel, D. & Wegener, G. *Wood: chemistry, ultrastructure, reactions*. (Walter de Gruyter, 2011).
3. Rho, J.-Y., Kuhn-Spearing, L. & Zioupos, P. Mechanical properties and the hierarchical structure of bone. *Med. Eng. Phys.* **20**, 92–102 (1998).
4. Fleischli, F. D., Dietiker, M., Borgia, C. & Spolenak, R. The influence of internal length scales on mechanical properties in natural nanocomposites: a comparative study on inner layers of seashells. *Acta Biomater.* **4**, 1694–1706 (2008).
5. Habibi, Y., Lucia, L. A. & Rojas, O. J. Cellulose nanocrystals: chemistry, self-assembly, and applications. *Chem. Rev.* **110**, 3479–3500 (2010).
6. Priestly, E. *Introduction to liquid crystals*. (Springer Science & Business Media, 2012).
7. De France, K. J., Yager, K. G., Hoare, T. & Cranston, E. D. Cooperative ordering and kinetics of cellulose nanocrystal alignment in a magnetic field. *Langmuir* **32**, 7564–7571 (2016).
8. O'sullivan, A. C. Cellulose: the structure slowly unravels. *Cellulose* **4**, 173–207 (1997).
9. Marchessault, R. H. & Sundararajan, P. R. Cellulose. in *The polysaccharides* 11–95 (Elsevier, 1983).
10. Sjostrom, E. *Wood chemistry: fundamentals and applications*. (Gulf professional publishing, 1993).
11. Heux, L., Dinand, E. & Vignon, M. R. Structural aspects in ultrathin cellulose microfibrils followed by 13C CP-MAS NMR. *Carbohydr. Polym.* **40**, 115–124 (1999).
12. Hieta, K., Kuga, S. & Usuda, M. Electron staining of reducing ends evidences a parallel-chain structure in Valonia cellulose. *Biopolym. Orig. Res. Biomol.* **23**, 1807–1810 (1984).
13. Usov, I. *et al.* Understanding nanocellulose chirality and structure–properties relationship at the single fibril level. *Nat. Commun.* **6**, 1–11 (2015).
14. Giasson, J. Etudes microscopiques d'helicoides de systemes cellulosiques in vitro. (1997).
15. Liang, C. Y. & Marchessault, R. H. Infrared spectra of crystalline polysaccharides. I. Hydrogen bonds in native celluloses. *J. Polym. Sci.* **37**, 385–395 (1959).

16. Kondo, T. Hydrogen bonds in cellulose and cellulose derivatives. in *Polysaccharides: Structural diversity and functional versatility* 131–172 (Marcel Dekker, New York, 1998).
17. Cousins, S. K. & Brown Jr, R. M. Cellulose I microfibril assembly: computational molecular mechanics energy analysis favours bonding by van der Waals forces as the initial step in crystallization. *Polymer (Guildf).* **36**, 3885–3888 (1995).
18. Xu, X. *et al.* Cellulose nanocrystals vs. cellulose nanofibrils: a comparative study on their microstructures and effects as polymer reinforcing agents. *ACS Appl. Mater. Interfaces* **5**, 2999–3009 (2013).
19. Kalia, S., Kaith, B. S. & Kaur, I. *Cellulose fibers: bio-and nano-polymer composites: green chemistry and technology*. (Springer Science & Business Media, 2011).
20. Brown Jr, R. M. The biosynthesis of cellulose. *J. Macromol. Sci. Part A Pure Appl. Chem.* **33**, 1345–1373 (1996).
21. Moon, R. J., Martini, A., Nairn, J., Simonsen, J. & Youngblood, J. Cellulose nanomaterials review: structure, properties and nanocomposites. *Chem. Soc. Rev.* **40**, 3941–3994 (2011).
22. Turbak, A. F., Snyder, F. W. & Sandberg, K. R. Microfibrillated cellulose. (1981).
23. Josset, S. *et al.* Energy consumption of the nanofibrillation of bleached pulp, wheat straw and recycled newspaper through a grinding process. *Nord. Pulp Pap. Res. J.* **29**, 167–175 (2014).
24. Favier, V. *et al.* Nanocomposite materials from latex and cellulose whiskers. *Polym. Adv. Technol.* **6**, 351–355 (1995).
25. Wang, Q. Q. *et al.* Morphological development of cellulose fibrils of a bleached eucalyptus pulp by mechanical fibrillation. *Cellulose* **19**, 1631–1643 (2012).
26. Wågberg, L. *et al.* The build-up of polyelectrolyte multilayers of microfibrillated cellulose and cationic polyelectrolytes. *Langmuir* **24**, 784–795 (2008).
27. Saito, T., Nishiyama, Y., Putaux, J.-L., Vignon, M. & Isogai, A. Homogeneous suspensions of individualized microfibrils from TEMPO-catalyzed oxidation of native cellulose. *Biomacromolecules* **7**, 1687–1691 (2006).
28. El-Saied, H., Basta, A. H. & Gobran, R. H. Research progress in friendly environmental technology for the production of cellulose products (bacterial cellulose and its application). *Polym. Plast. Technol. Eng.* **43**, 797–820 (2004).

29. Brown, R. M., Willison, J. H. & Richardson, C. L. Cellulose biosynthesis in Acetobacter xylinum: visualization of the site of synthesis and direct measurement of the in vivo process. *Proc. Natl. Acad. Sci.* **73**, 4565–4569 (1976).
30. Yamanaka, S. & Sugiyama, J. Structural modification of bacterial cellulose. *Cellulose* **7**, 213–225 (2000).
31. Bodin, A., Concaro, S., Brittberg, M. & Gatenholm, P. Bacterial cellulose as a potential meniscus implant. *J. Tissue Eng. Regen. Med.* **1**, 406–408 (2007).
32. Klemm, D., Schumann, D., Udhardt, U. & Marsch, S. Bacterial synthesized cellulose—artificial blood vessels for microsurgery. *Prog. Polym. Sci.* **26**, 1561–1603 (2001).
33. Stanisławska, A. Bacterial nanocellulose as a microbiological derived nanomaterial. *Adv. Mater. Sci.* **16**, 45–57 (2016).
34. Nogi, M. & Yano, H. Transparent nanocomposites based on cellulose produced by bacteria offer potential innovation in the electronics device industry. *Adv. Mater.* **20**, 1849–1852 (2008).
35. Matos Ruiz, M., Cavaille, J. Y., Dufresne, A., Gerard, J. F. & Graillat, C. Processing and characterization of new thermoset nanocomposites based on cellulose whiskers. *Compos. Interfaces* **7**, 117–131 (2000).
36. Honary, S. & Zahir, F. Effect of zeta potential on the properties of nano-drug delivery systems-a review (Part 1). *Trop. J. Pharm. Res.* **12**, 255–264 (2013).
37. Revol, J.-F., Bradford, H., Giasson, J., Marchessault, R. H. & Gray, D. G. Helicoidal self-ordering of cellulose microfibrils in aqueous suspension. *Int. J. Biol. Macromol.* **14**, 170–172 (1992).
38. Poaty, B., Vardanyan, V., Wilczak, L., Chauve, G. & Riedl, B. Modification of cellulose nanocrystals as reinforcement derivatives for wood coatings. *Prog. Org. Coatings* **77**, 813–820 (2014).
39. Pei, A., Malho, J.-M., Ruokolainen, J., Zhou, Q. & Berglund, L. A. Strong nanocomposite reinforcement effects in polyurethane elastomer with low volume fraction of cellulose nanocrystals. *Macromolecules* **44**, 4422–4427 (2011).
40. Zhou, C. *et al.* Electrospun bio-nanocomposite scaffolds for bone tissue engineering by cellulose nanocrystals reinforcing maleic anhydride grafted PLA. *ACS Appl. Mater. Interfaces* **5**, 3847–3854 (2013).
41. Rojas, O. J., Montero, G. A. & Habibi, Y. Electrospun nanocomposites from polystyrene loaded with cellulose nanowhiskers. *J. Appl. Polym. Sci.* **113**, 927–935 (2009).

42. Tashiro, K. & Kobayashi, M. Theoretical evaluation of three-dimensional elastic constants of native and regenerated celluloses: role of hydrogen bonds. *Polymer (Guildf).* **32**, 1516–1526 (1991).
43. Rusli, R. & Eichhorn, S. J. Determination of the stiffness of cellulose nanowhiskers and the fiber-matrix interface in a nanocomposite using Raman spectroscopy. *Appl. Phys. Lett.* **93**, 33111 (2008).
44. Cheng, M., Chen, W. & Weerasooriya, T. Mechanical properties of Kevlar® KM2 single fiber. *J. Eng. Mater. Technol.* **127**, 197–203 (2005).
45. Messier, D. R. & Patel, P. J. High modulus glass fibers. *J. Non. Cryst. Solids* **182**, 271–277 (1995).
46. Favier, V., Cavaille, J. Y., Canova, G. R. & Shrivastava, S. C. Mechanical percolation in cellulose whisker nanocomposites. *Polym. Eng. Sci.* **37**, 1732–1739 (1997).
47. Azizi Samir, M. A. S., Alloin, F. & Dufresne, A. Review of recent research into cellulosic whiskers, their properties and their application in nanocomposite field. *Biomacromolecules* **6**, 612–626 (2005).
48. Lagerwall, J. P. F. & Scalia, G. A new era for liquid crystal research: Applications of liquid crystals in soft matter nano-, bio-and microtechnology. *Curr. Appl. Phys.* **12**, 1387–1412 (2012).
49. Lagerwall, J. P. F. *et al.* Cellulose nanocrystal-based materials: from liquid crystal self-assembly and glass formation to multifunctional thin films. *NPG Asia Mater.* **6**, e80 (2014).
50. Domingues, R. M. A., Gomes, M. E. & Reis, R. L. The potential of cellulose nanocrystals in tissue engineering strategies. *Biomacromolecules* **15**, 2327–2346 (2014).
51. Yablonovitch, E. Photonic band-gap structures. *JOSA B* **10**, 283–295 (1993).
52. Gray, G. W. Liquid Crystals: Overview. in *Encyclopedia of Materials: Science and Technology* (eds. Buschow, K. H. J. et al.) 4570–4578 (Elsevier, 2001). doi:https://doi.org/10.1016/B0-08-043152-6/00799-3
53. Kumar, S. *Chemistry of discotic liquid crystals: from monomers to polymers*. (CRC press, 2016).
54. Priestley, E. B. Liquid crystal mesophases. in *Introduction to Liquid Crystals* 1–13 (Springer, 1975).
55. Xu, S., Girouard, N., Schueneman, G., Shofner, M. L. & Meredith, J. C. Mechanical and thermal properties of waterborne epoxy composites containing cellulose nanocrystals. *Polymer (Guildf).* **54**, 6589–6598 (2013).

56. Chen, W. & Gray, D. G. Interfacial tension between isotropic and anisotropic phases of a suspension of rodlike particles. *Langmuir* **18**, 633–637 (2002).
57. Khandelwal, M. & Windle, A. Origin of chiral interactions in cellulose supra-molecular microfibrils. *Carbohydr. Polym.* **106**, 128–131 (2014).
58. Revol, J.-F. *et al.* Chiral nematic suspensions of cellulose crystallites; phase separation and magnetic field orientation. *Liq. Cryst.* **16**, 127–134 (1994).
59. Ureña-Benavides, E. E., Ao, G., Davis, V. A. & Kitchens, C. L. Rheology and phase behavior of lyotropic cellulose nanocrystal suspensions. *Macromolecules* **44**, 8990–8998 (2011).
60. Wang, P.-X., Hamad, W. Y. & MacLachlan, M. J. Structure and transformation of tactoids in cellulose nanocrystal suspensions. *Nat. Commun.* **7**, 1–8 (2016).
61. Majoinen, J., Kontturi, E., Ikkala, O. & Gray, D. G. SEM imaging of chiral nematic films cast from cellulose nanocrystal suspensions. *Cellulose* **19**, 1599–1605 (2012).
62. De Gennes, P.-G. & Prost, J. *The physics of liquid crystals*. **83**, (Oxford university press, 1993).
63. Wichterle, O. & Lim, D. Hydrophilic gels for biological use. *Nature* **185**, 117–118 (1960).
64. Yang, B., Wei, Z., Chen, X., Wei, K. & Bian, L. Manipulating the mechanical properties of biomimetic hydrogels with multivalent host–guest interactions. *J. Mater. Chem. B* **7**, 1726–1733 (2019).
65. Montheard, J.-P., Chatzopoulos, M. & Chappard, D. 2-hydroxyethyl methacrylate (HEMA): chemical properties and applications in biomedical fields. *J. Macromol. Sci. Part C Polym. Rev.* **32**, 1–34 (1992).
66. Bat, E. Hydroxyethylmethacrylate based nanocomposite hydrogels with tunable pore architecture. *J. Turkish Chem. Soc. Sect. A Chem.* **3**, 607–622 (2016).
67. Hoffman, A. S. Hydrogels for biomedical applications. *Adv. Drug Deliv. Rev.* **64**, 18–23 (2012).
68. Calvert, P. Hydrogels for soft machines. *Adv. Mater.* **21**, 743–756 (2009).
69. Stoy, V., Wichterle, O. & Stoy, A. Soft contact lens from a macromolecular block copolymer. (1978).
70. Lu, S. & Anseth, K. S. Photopolymerization of multilaminated poly (HEMA) hydrogels for controlled release. *J. Control. release* **57**, 291–300 (1999).
71. Matyjaszewski, K. & Davis, T. P. *Handbook of radical polymerization*. (John Wiley & Sons, 2003).

72. Hirao, A., Kato, H., Yamaguchi, K. & Nakahama, S. Polymerization of monomers containing functional groups protected by trialkylsilyl groups. 5. Synthesis of poly (2-hydroxyethyl methacrylate) with a narrow molecular weight distribution by means of anionic living polymerization. *Macromolecules* **19**, 1294–1299 (1986).
73. Chu, H. & Fu, D. Preparation of poly (hydroxyethyl methacrylate) and poly (hydroxypropyl methacrylate) latices. *Macromol. Rapid Commun.* **19**, 107–110 (1998).
74. Miyazaki, T., Yamaoka, K., Gong, J. P. & Osada, Y. Hydrogels with crystalline or liquid crystalline structure. *Macromol. Rapid Commun.* **23**, 447–455 (2002).
75. Marolt, M. & Jaglicic, Z. Superparamagnetic materials. *Semin. Mestrado, Univ. Ljubljana, Slov.* (2014).
76. Majetich, S. A., Wen, T. & Booth, R. A. Functional magnetic nanoparticle assemblies: formation, collective behavior, and future directions. *ACS Nano* **5**, 6081–6084 (2011).
77. Răcuciu, M., Creangă, D. E. & Airinei, A. Citric-acid-coated magnetite nanoparticles for biological applications. *Eur. Phys. J. E* **21**, 117–121 (2006).
78. Berry, C. C. Progress in functionalization of magnetic nanoparticles for applications in biomedicine. *J. Phys. D. Appl. Phys.* **42**, 224003 (2009).
79. Otsuka, H., Nagasaki, Y. & Kataoka, K. PEGylated nanoparticles for biological and pharmaceutical applications. *Adv. Drug Deliv. Rev.* **55**, 403–419 (2003).
80. Hatakeyama, M. *et al.* A two-step ligand exchange reaction generates highly water-dispersed magnetic nanoparticles for biomedical applications. *J. Mater. Chem.* **21**, 5959–5966 (2011).
81. Colombo, M. *et al.* Biological applications of magnetic nanoparticles. *Chem. Soc. Rev.* **41**, 4306–4334 (2012).
82. Raj, K. & Moskowitz, R. Commercial applications of ferrofluids. *J. Magn. Magn. Mater.* **85**, 233–245 (1990).
83. Obata, K., Tajima, H., Yohda, M. & Matsunaga, T. Recent developments in laboratory automation using magnetic particles for genome analysis. *Pharmacogenomics* **3**, 697–708 (2002).
84. Brown, G. D. & Gordon, S. Immune recognition of fungal β-glucans. *Cell. Microbiol.* **7**, 471–479 (2005).
85. Kralj, S. & Makovec, D. Magnetic assembly of superparamagnetic iron oxide nanoparticle clusters into nanochains and nanobundles. *ACS Nano* **9**, 9700–9707 (2015).
86. Daniel, I. M., Ishai, O., Daniel, I. M. & Daniel, I. *Engineering mechanics of composite materials*. **3**, (Oxford university press New York, 1994).

87. Clyne, T. W. & Hull, D. *An introduction to composite materials*. (Cambridge university press, 2019).
88. Besseau, L. & Bouligand, Y. The twisted collagen network of the box-fish scutes. *Tissue Cell* **30**, 251–260 (1998).
89. Nikolov, S. *et al.* Revealing the design principles of high-performance biological composites using ab initio and multiscale simulations: the example of lobster cuticle. *Adv. Mater.* **22**, 519–526 (2010).
90. Weaver, J. C. *et al.* The stomatopod dactyl club: a formidable damage-tolerant biological hammer. *Science (80-.).* **336**, 1275–1280 (2012).
91. Tatsumi, M., Teramoto, Y. & Nishio, Y. Polymer composites reinforced by locking-in a liquid-crystalline assembly of cellulose nanocrystallites. *Biomacromolecules* **13**, 1584–1591 (2012).
92. Wang, P. X., Hamad, W. Y. & MacLachlan, M. J. Liquid Crystalline Tactoidal Microphases in Ferrofluids: Spatial Positioning and Orientation by Magnetic Field Gradients. *Chem* **5**, 681–692 (2019).
93. Massart, R. Preparation of aqueous magnetic liquids in alkaline and acidic media. *IEEE Trans. Magn.* **17**, 1247–1248 (1981).
94. Talbot, D., Abramson, S., Griffete, N. & Bee, A. pH-sensitive magnetic alginate/γ-Fe2O3 nanoparticles for adsorption/desorption of a cationic dye from water. *J. Water Process Eng.* **25**, 301–308 (2018).
95. Muthukumar, M. Ordinary–extraordinary transition in dynamics of solutions of charged macromolecules. *Proc. Natl. Acad. Sci.* **113**, 12627–12632 (2016).
96. Elazzouzi-Hafraoui, S. *et al.* The shape and size distribution of crystalline nanoparticles prepared by acid hydrolysis of native cellulose. *Biomacromolecules* **9**, 57–65 (2008).
97. Foner, S. Versatile and sensitive vibrating-sample magnetometer. *Rev. Sci. Instrum.* **30**, 548–557 (1959).
98. Wahajuddin, S. A. Superparamagnetic iron oxide nanoparticles: magnetic nanoplatforms as drug carriers. *Int. J. Nanomedicine* **7**, 3445 (2012).
99. Roylance, D. Stress-Strain curves. *Department of Materials Science and Engineering, Massachusetts Institute of Technology* 14 (2001). Available at: http://web.mit.edu/course/3/3.11/www/modules/ss.pdf.
100. Hobzova, R., Duskova-Smrckova, M., Michalek, J., Karpushkin, E. & Gatenholm, P. Methacrylate hydrogels reinforced with bacterial cellulose. *Polym. Int.* **61**, 1193–1201 (2012).

101. Bonderer, L. J., Studart, A. R. & Gauckler, L. J. Bioinspired design and assembly of platelet reinforced polymer films. *Science (80-.).* **319**, 1069–1073 (2008).
102. Gulsen, D. & Chauhan, A. Effect of water content on transparency, swelling, lidocaine diffusion in p-HEMA gels. *J. Memb. Sci.* **269**, 35–48 (2006).
103. Paula, F. L. de O. *et al.* Gravitational and magnetic separation in self-assembled clay-ferrofluid nanocomposites. *Brazilian J. Phys.* **39**, 163–170 (2009).
104. Quilliet, C., Fabre, P. & Cabuil, V. Doping of lyotropic smectics with nonmagnetic particles: comparison with ferrosmectics. *J. Phys. Chem.* **97**, 287–289 (1993).
105. Brochard, F. & De Gennes, P. G. Theory of magnetic suspensions in liquid crystals. *J. Phys.* **31**, 691–708 (1970).
106. Yadav, S. P., Yadav, K., Lahiri, J. & Singh Parmar, A. Ferroelectric liquid crystal nanocomposites: recent development and future perspective. *Liq. Cryst. Rev.* **6**, 143–169 (2018).
107. Ménager, C. *et al.* Osmotic equilibrium between an ionic magnetic fluid and an electrostatic lamellar phase. *Langmuir* **12**, 3516–3522 (1996).
108. Ackerman, P. J., Boyle, T. & Smalyukh, I. I. Squirming motion of baby skyrmions in nematic fluids. *Nat. Commun.* (2017). doi:10.1038/s41467-017-00659-5
109. Gupta, A. K. & Gupta, M. Synthesis and surface engineering of iron oxide nanoparticles for biomedical applications. *Biomaterials* **26**, 3995–4021 (2005).

8. Appendix 1

Figure 46 depicts stress-strain curves for hydrogels of type *H*. None of the curves were omitted in the final average curve.

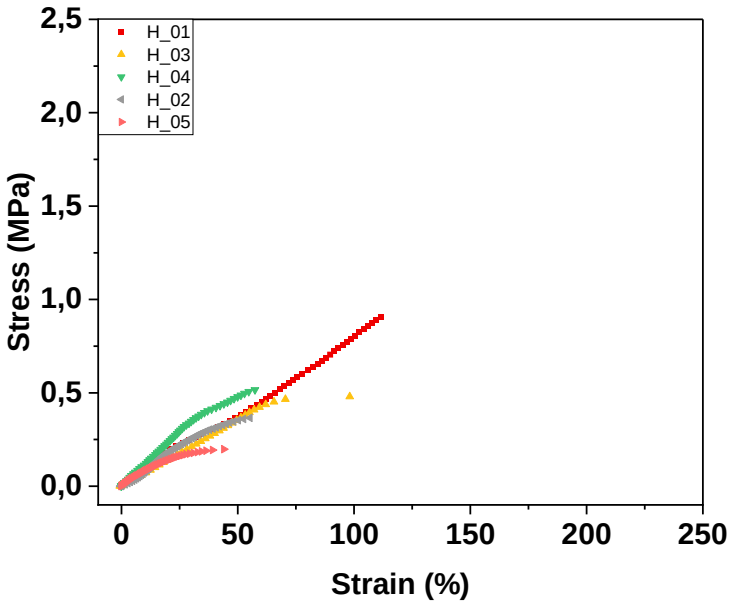

Figure 46: Stress-strain curves for individual H hydrogel nanocomposites

Figure 47 depicts stress-strain curves for hydrogels of type *HC*. None of the curves were omitted in the final average curve.

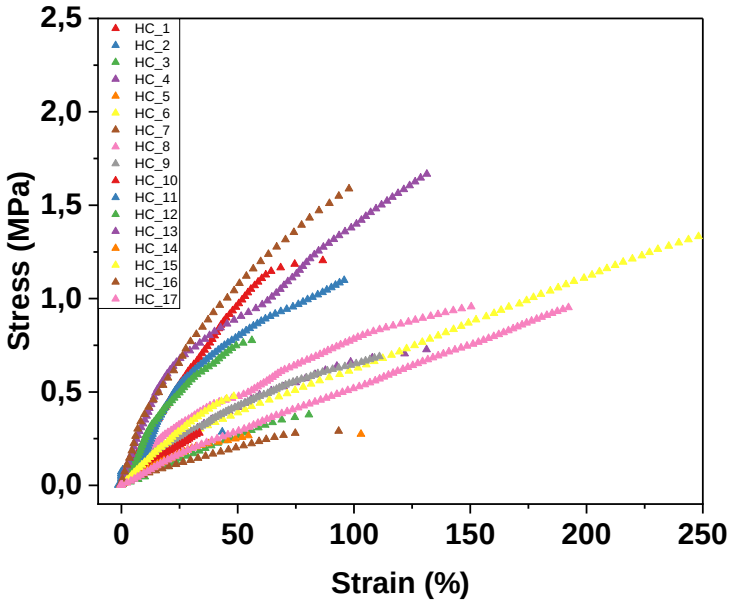

Figure 47: Stress-strain curves for individual HC hydrogel nanocomposites

Figure 48 depicts stress-strain curves for hydrogels of type *HC_4h*. Curves representing specimens 02 and 013 were omitted in the final average curve due to slippage and significant deviation of its behavior in comparison to the other samples, respectively.

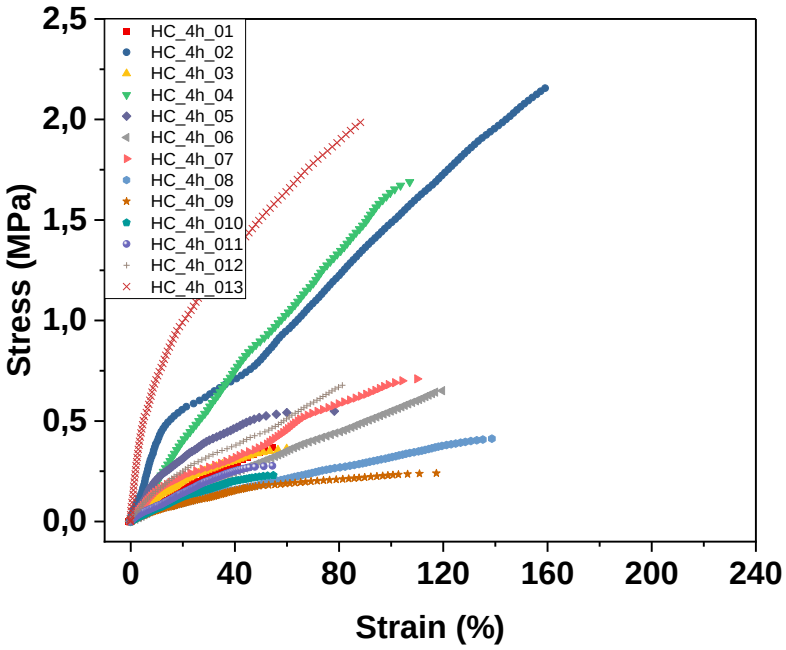

Figure 48: Stress-strain curves for individual HC_4h hydrogel nanocomposites

Figure 49 depicts stress-strain curves for hydrogels of type *HC$_{mg}$_4h*. Curves representing specimens 08 and 010 were omitted in the final average curve due significant deviation in comparison to the other samples.

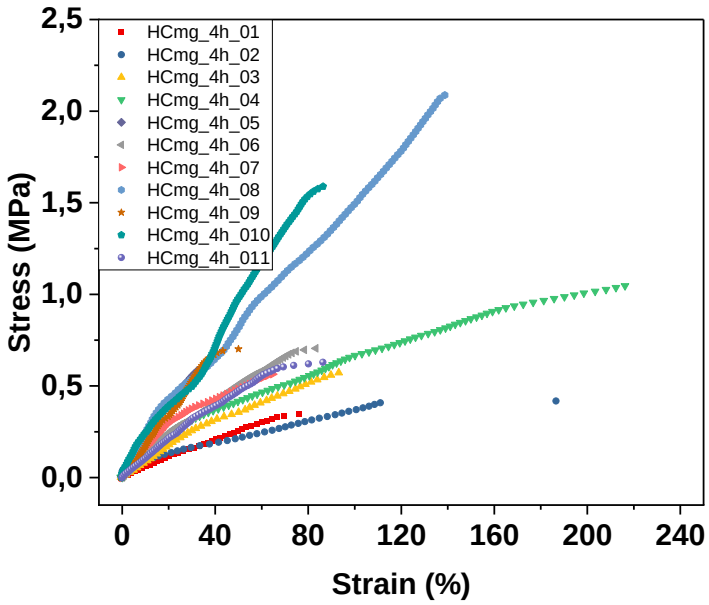

Figure 49: Stress-strain curves for individual HC$_{mg}$_4h hydrogel nanocomposites

Figure 50 depicts stress-strain curves for hydrogels of type *HC_15h*. Curves representing specimens *06* and *013* were omitted in the final average curve due significant deviation in comparison to the other samples.

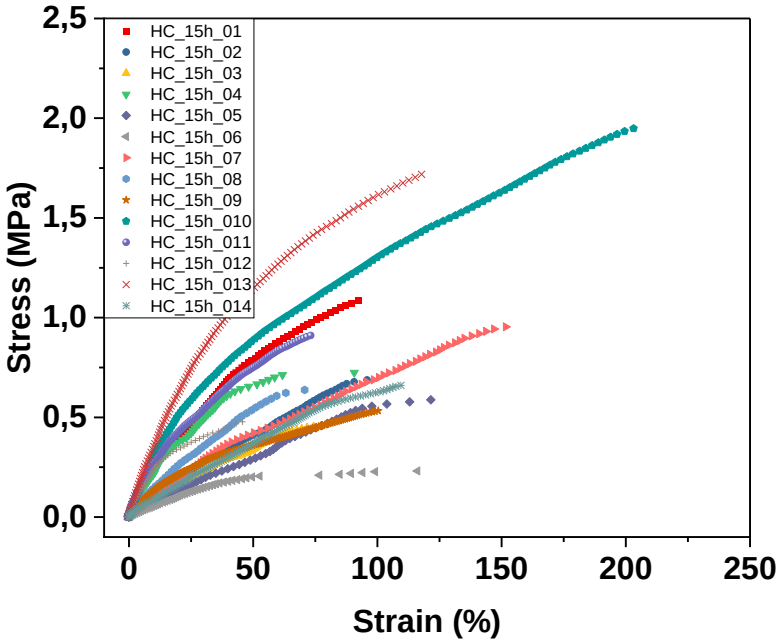

Figure 50: Stress-strain curves for individual HC_15h hydrogel nanocomposites

Figure 51 depicts stress-strain curves for hydrogels of type *HC_15h*. Curves representing specimens *09* and *011* were omitted in the final average curve due significant deviation in comparison to the other samples.

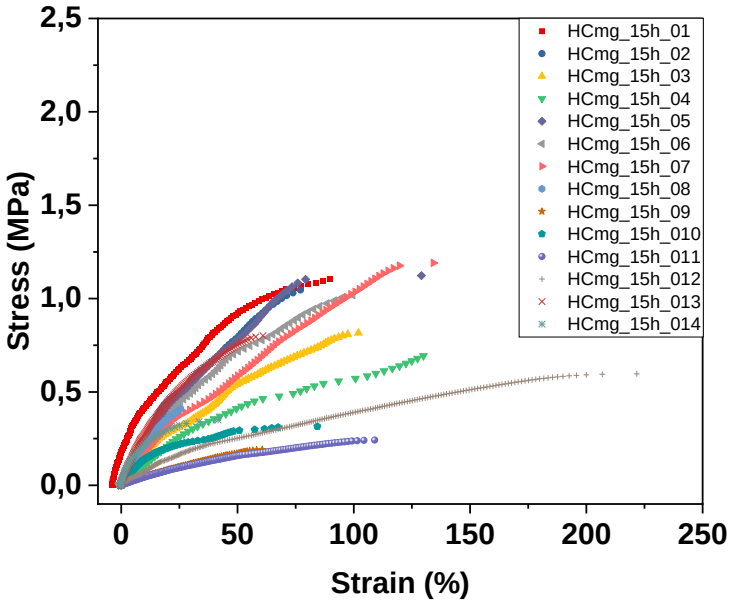

Figure 51: Stress-strain curves for individual HC_{mg}_15h hydrogel nanocomposites

Table 3: Average Young's moduli of the studied hydrogels and corresponding standard deviations

specimen	Young's modulus (kPa)	standard deviation (kPa)
H	12,2	0,1
HC	15,0	0,3
HC_4h	11,6	0,2
HC_{mg}_4h	12,7	0,1
HC_15h	17,1	0,3
HC_{mg}_15h	21,3	0,3

Table 4: Average Ultimate strength of the studied hydrogels and corresponding standard deviations

specimen	Ultimate strength (kPa)	standard deviation (kPa)
H	494,0	237,4
HC	811,3	482,9
HC_4h	532,7	398,0
HC_{mg}_4h	617,8	189,8
HC_15h	802,5	387,7
HC_{mg}_15h	786,7	301,1

Table 5: Mean weight content of free-water in specimens and corresponding standard deviations

specimen	mean W_0 (mg)	mean W_x (mg)	mean solid content wt. %	mean$_{H2O}$ wt. %	std. deviation
H	55,9	28,5	50,9 %	**49,1 %**	**2,5 %**
HC	54,0	25,2	46,6 %	**53,4 %**	**1,8 %**
HC_4h	80,6	39,7	49,3 %	**50,7 %**	**2,1 %**
HC_{mg}_4h	91,7	40,4	44,0 %	**56,0 %**	**2,2 %**
HC_15h	84,3	40,8	48,4 %	**51,6 %**	**2,0 %**
HC_{mg}_15h	78,8	38,7	49,1 %	**50,9 %**	**2,3 %**